



Patchy Forsterite Clouds in the Atmospheres of Two Highly Variable Exoplanet Analogs

Johanna M. Vos¹, Ben Burningham², Jacqueline K. Faherty¹, Shereyn Alejandro^{1,3}, Eileen Gonzales^{4,16}, Emily Calamari^{1,5}, Daniella Bardalez Gagliuffi^{1,6}, Channon Visscher^{7,8}, Xianyu Tan⁹, Caroline V. Morley¹⁰, Mark Marley¹¹, Marina E. Gemma^{12,13}, Niall Whiteford¹, Josefina Gaarn¹⁴, and Grace Park¹⁵

¹ Department of Astrophysics, American Museum of Natural History, New York, NY 10024, USA; jvos@amnh.org

² Centre for Astrophysics Research, Department of Physics, Astronomy and Mathematics, University of Hertfordshire, Hatfield AL10 9AB, UK

³ Hunter College, City University of New York, 695 Park Avenue, New York, NY 10065, USA

⁴ Department of Astronomy and Carl Sagan Institute, Cornell University, 122 Sciences Drive, Ithaca, NY 14853, USA

⁵ The Graduate Center, City University of New York, New York, NY 10016, USA

⁶ Department of Physics & Astronomy, Amherst College, 25 East Drive, Amherst, MA 01003, USA

⁷ Chemistry & Planetary Sciences, Dordt University, Sioux Center, IA, USA

⁸ Center for Extrasolar Planetary Systems, Space Science Institute, Boulder, CO, USA

⁹ Atmospheric, Ocean, and Planetary Physics, Department of Physics, University of Oxford, UK

¹⁰ Department of Astronomy, University of Texas at Austin, Austin, TX 78712, USA

¹¹ Department of Planetary Sciences and Lunar and Planetary Laboratory, University of Arizona, Tucson, AZ, USA

¹² Department of Earth and Environmental Sciences, Columbia University, New York, NY 10027, USA

¹³ Department of Earth and Planetary Sciences, American Museum of Natural History, New York, NY 10024, USA

¹⁴ Centre for Astrophysics Research, School of Physics, Astronomy and Mathematics, University of Hertfordshire, Hatfield AL10 9AB, UK

¹⁵ Palisades Park High School, Palisades Park, NJ 07650, USA

Received 2022 October 26; revised 2022 December 9; accepted 2022 December 12; published 2023 February 21

Abstract

We present an atmospheric retrieval analysis of a pair of highly variable, ~ 200 Myr old, early T type planetary-mass exoplanet analogs SIMP J01365662+0933473 and 2MASS J21392676+0220226 using the Brewster retrieval framework. Our analysis, which makes use of archival 1–15 μm spectra, finds almost identical atmospheres for both objects. For both targets, we find that the data is best described by a patchy, high-altitude forsterite (Mg_2SiO_4) cloud above a deeper, optically thick iron (Fe) cloud. Our model constrains the cloud properties well, including the cloud locations and cloud particle sizes. We find that the patchy forsterite slab cloud inferred from our retrieval may be responsible for the spectral behavior of the observed variability. Our retrieved cloud structure is consistent with the atmospheric structure previously inferred from spectroscopic variability measurements, but clarifies this picture significantly. We find consistent C/O ratios for both objects, which supports their formation within the same molecular cloud in the Carina-Near moving group. Finally, we note some differences in the constrained abundances of H_2O and CO, which may be caused by data quality and/or astrophysical processes such as auroral activity and their differing rotation rates. The results presented in this work provide a promising preview of the detail with which we will characterize extrasolar atmospheres with JWST, which will yield higher-quality spectra across a wider wavelength range.

Unified Astronomy Thesaurus concepts: [Brown dwarfs \(185\)](#); [T dwarfs \(1679\)](#); [Exoplanet atmospheres \(487\)](#); [Exoplanet atmospheric composition \(2021\)](#); [Exoplanet astronomy \(486\)](#); [Exoplanet atmospheric variability \(2020\)](#)

1. Introduction

Since 1995, over 5000 planets orbiting other stars have been discovered using a variety of techniques. Of particular interest are the small number of imaged exoplanets that offer the most direct view into their atmospheres (e.g., Chauvin et al. 2004; Marois et al. 2008; Lagrange et al. 2010; Macintosh et al. 2015; Bohn et al. 2020, 2021). Current and forthcoming telescopes such as the James Webb Space Telescope (JWST) and 30 m telescopes (e.g., the Extremely Large Telescope; first light expected ~ 2027) will enable direct exoplanet studies (e.g., Carter et al. 2022), but the interpretation of these results will hinge on a thorough understanding of their complex atmospheres. In the same time frame, a large number of brown dwarfs have been discovered that overlap in mass, age, and

temperature with the directly imaged exoplanets (Faherty et al. 2016; Liu et al. 2016). These isolated exoplanet analogs are much easier to study without the glare of a bright host star, and offer crucial insight into the nature of extrasolar atmospheres.

Condensate clouds have emerged as one of the most confounding issues for attempts to characterize extrasolar atmospheres in detail. These clouds are predicted to form in atmospheres with temperatures below ~ 2200 K (Burrows et al. 1997; Ackerman & Marley 2001; Helling et al. 2008; Allard et al. 2012), and dramatically shape the observed appearance of brown dwarfs and directly imaged exoplanets. For example, the red near-IR colors of L dwarfs are thought to be caused by the presence of silicate clouds while the blue near-IR colors of T dwarfs are caused by those same clouds sinking below the photosphere (Ackerman & Marley 2001; Saumon & Marley 2008).

Variability monitoring is a powerful probe of extrasolar atmospheres. Solar system gas giants, giant exoplanets, and brown dwarfs exhibit temporal variability in broadband emission and spectra as they rotate. This observed photometric and spectroscopic variability is generally thought to be driven

¹⁶ 51 Pegasi b Postdoctoral Fellow.

by the presence of inhomogeneous clouds. In the case of Jupiter, unresolved observations at $5\ \mu\text{m}$ reveal periodic variability with amplitudes exceeding 20% (Gelino & Marley 2000; Ge et al. 2019), caused by a range of inhomogeneous atmospheric features such as the Great Red Spot, the North Equatorial Belt, and the North Temperate Belt (Ge et al. 2019). Beyond the solar system, these kinds of observations have been carried out for a large number of field brown dwarfs (Buenzli et al. 2014; Radigan et al. 2014; Metchev et al. 2015), isolated exoplanet analogs (Biller et al. 2015, 2018; Lew et al. 2016; Vos et al. 2019, 2022), and a smaller sample of wide orbit companions (Zhou et al. 2016, 2019, 2020). Large surveys have shown that variability is common (Radigan et al. 2014; Metchev et al. 2015), particularly among the young, low-gravity sample (Vos et al. 2019, 2022). In-depth spectroscopic monitoring studies, many of which make use of the WFC3 instrument on the Hubble Space Telescope (HST), have also revealed clues on the vertical cloud structure in extrasolar atmospheres (e.g., Apai et al. 2013; Buenzli et al. 2015; Lew et al. 2016), with wavelength-dependent amplitudes and phase shifts suggesting the presence of regions of thin and thick cloud cover.

Atmospheric retrieval algorithms have also emerged as a powerful probe of extrasolar atmospheres, complementary to the information that can be gleaned from variability monitoring observations. Originally developed for remote sensing solar system atmospheres, atmospheric retrievals have recently been used to study exoplanet and brown dwarf atmospheres (e.g., Madhusudhan & Seager 2009; Lee et al. 2012; Line et al. 2014; Burningham et al. 2017, 2021; MacDonald & Madhusudhan 2017; Mollière et al. 2019, 2020; Barstow & Heng 2020; Kitzmann et al. 2020). In comparison to traditional approaches, whereby spectra of brown dwarfs and exoplanets are interpreted via comparison with precomputed grids of self-consistent model atmospheres, atmospheric retrievals allow for a more efficient exploration of the parameter space with fewer initial assumptions. This data-driven technique allows for empirical constraints to be placed directly on key atmospheric parameters.

The Brewster retrieval code (Burningham et al. 2017) was specifically designed to capture the complexity of clouds in giant extrasolar atmospheres, and its effectiveness has been demonstrated across the L and T spectral sequence (Burningham et al. 2017, 2021; Gonzales et al. 2020, 2021; Calamari et al. 2022; J. Gaarn et al. 2023, in preparation). Burningham et al. (2021) in particular demonstrated the power of this algorithm when combined with wide wavelength spectroscopy, finding that the atmosphere of the mid-L dwarf 2MASSW J2224438-015852 (2MASS 2224-01 hereafter) is best described by a rather complex model that includes enstatite (MgSiO_3) and quartz (SiO_2) cloud layers at shallow pressures, combined with a deeper iron (Fe) cloud deck.

To date, the techniques of time-resolved variability monitoring and atmospheric retrievals have been applied separately to reveal extrasolar atmospheres. In this work, we present the first attempt to combine the information gleaned from each technique by performing atmospheric retrievals on a pair of exoplanet analogs whose variability properties have been studied in detail. By combining results gained from our retrievals with past studies of the time-resolved behavior of

their atmospheres, our goal is to provide the clearest view to date of two extrasolar atmospheres.

2. Twin Variable Worlds: SIMP J0136+09 and 2MASS J2139+02

The T2.5 dwarf SIMP J01365662+0933473 (SIMP J0136+09 hereafter) was the first brown dwarf known to display repeatable, periodic variability due to inhomogeneous condensate clouds. The initial discovery paper by Artigau et al. (2009) revealed a rotation period of ~ 2.4 hr, a peak-to-peak J -band amplitude of ~ 50 mmag, and significant light-curve evolution between consecutive nights. Yang et al. (2016) refined the rotation period measurement to 2.414 ± 0.078 hr based on photometric monitoring with the Spitzer Space Telescope. Vos et al. (2017) determined that SIMP J0136+09 is inclined close to equator-on ($i = 80_{-12}^{+19}$ °) based on its rotation period and a $v \sin i$ measurement. Kao et al. (2016) detected circularly polarized emission in the 4–8 GHz band consistent with auroral activity, and estimated a magnetic field strength of >2.5 kG. Gagné et al. (2017) identified SIMP J0136+09 as a member of the ~ 200 Myr Carina-Near moving group, and estimate a mass of $12.7 \pm 1.0 M_{\text{Jup}}$, placing it at the nominal boundary between planets and brown dwarfs.

The T1.5 dwarf 2MASS J21392676+0220226 (2MASS J2139+02 hereafter) has emerged as a twin to SIMP J0136+09, sharing many observable and physical properties. Radigan et al. (2012) first reported extremely high-amplitude near-IR variability in 2MASS J2139+02. Using multiple epochs of ground-based monitoring observations, they measured peak-to-peak amplitudes as high as 26% in J band and a period of 7.721 ± 0.005 hr. This extremely high amplitude is matched only by VHS J125601.92–125723.9 B (Bowler et al. 2020), a late-type L dwarf comoving with a young late-M binary system, and thus represents a strong outlier in the population of known variables. By examining the observed amplitudes across different bands, Radigan et al. (2012) attributed the observed variability to be due to patches of thin and thick clouds. Vos et al. (2017) determined that 2MASS J2139+02 is inclined equator-on by combining its rotation period with a $v \sin i$ measurement. A new parallax measurement for 2MASS J2139+02 reported by Zhang et al. (2021b) revealed that 2MASS J2139+02 is also a member of the Carina-Near moving group, making it a true sibling of SIMP J0136+09.

As the first two high-amplitude L/T transition variables known, 2MASS J2139+02 and SIMP J0136+09 have often been studied side by side. Apai et al. (2013) followed up both objects with spectroscopic variability monitoring using the HST WFC3 grism mode. These observations revealed spectroscopic variations that were remarkably similar in both targets— J - and H -bands brightness variations with minimal color and spectral changes. The authors find that the observed color changes and spectral variations in both cases are best described by an atmosphere with a heterogeneous mixture of cool, thick clouds and warmer, thin clouds, as opposed to patches of cloudy and clear patches. The authors estimate a ~ 300 K temperature difference between the two cloud regions for SIMP J0136+09 and 2MASS J2139+02. More recently, Apai et al. (2017) obtained long-term monitoring of both objects using the Spitzer Space Telescope, finding that they both exhibit similar long-term light-curve evolution. They find that

the long-term behavior of their light curves can be explained by sinusoidally modulated zonal bands as well as a bright spot.

With their recent identifications as members of the Carina-Near association, the comparison of 2MASS J2139+02 and SIMP J0136+09 is even more fitting today. With similar ages, masses, and temperatures, this unique pair of objects allows us to examine the atmospheres of two objects that presumably share a formation history and subsequent evolution. In this paper, we employ the Brewster spectral retrieval framework to compare and contrast the constituents of their atmospheres.

3. Spectral Data

In order to gain the most comprehensive view of the atmospheres of SIMP J0136+09 and 2MASS J2139+02, we use the widest wavelength range available for both targets. For SIMP J0136+09, our spectrum is comprised of a 1–2.5 μm Infrared Telescope Facility (IRTF)/SpeX Prism spectrum ($R \sim 120$, signal-to-noise ratio, hereafter S/N, ~ 180 ; Burgasser et al. 2008), a 2.5–5 μm AKARI/Infrared Camera (IRC) spectrum reported by Sorahana et al. (2013) ($R \sim 100$, S/N ~ 9), and a 5–15 μm Spitzer/intensified Reticon spectrograph (IRS) spectrum presented by Filippazzo et al. (2015) ($R \sim 90$, S/N ~ 15). Our 2MASS J2139+02 spectrum consists of a 1–2.5 μm IRTF/SpeX spectrum from Burgasser et al. (2006) ($R \sim 120$, S/N ~ 170) and a 5–15 μm Spitzer/IRS spectrum presented by Suárez & Metchev (2022) ($R \sim 90$, S/N ~ 6). The near-infrared data for both sources was flux calibrated using their parallax and Two Micron All Sky Survey (2MASS) J photometry, while the AKARI/IRC and Spitzer/IRS spectra were already flux calibrated (Filippazzo et al. 2015; Suárez & Metchev 2022). We note that, for 2MASS J2139+02, while Suárez & Metchev (2022) corrected their Spitzer/IRS spectrum flux calibration to match Wide-field Infrared Survey Explorer W3-band photometry, we use the IRS instrumental flux calibration for this work.

4. Fundamental Parameters via SEDkit

We analyze the spectral energy distributions (SEDs) of our two targets to estimate their fundamental parameters, using the technique described in Filippazzo et al. (2015). Parameter values were determined using SEDKIT V1.2.4, which uses spectra, photometry, and parallax measurements to create a distance-calibrated SED in order to determine the bolometric luminosity, L_{bol} . This method uses photometric measurements to calibrate the spectral data. We use the same spectra detailed in Section 3, and the photometry and parallaxes shown in Table 1. Combining the L_{bol} value and age estimate, we use the Saumon & Marley (2008) hybrid cloud evolutionary models to estimate the radius, mass, $\log g$, and effective temperature (T_{eff}) of each target. We present these determined values in Table 1.

Our SED analysis highlights the similarities in the fundamental properties of SIMP J0136+09 and 2MASS J2139+02, with T_{eff} within ~ 150 K, masses that straddle the nominal boundary between planets and brown dwarfs, and almost identical radii. Investigating the atmospheres of this pair of twin worlds will offer insights on the diversity of extrasolar atmospheres.

5. Retrieval Framework

We perform atmospheric retrievals on our data using the Brewster framework (Burningham et al. 2017, 2021). We refer the reader to Burningham et al. (2017) for a complete

Table 1
Observed Properties and Derived Fundamental Parameters for 2MASS J2139+02 and SIMP J0136+09

Property	2MASS J2139+02	SIMP J0136+09	Reference
R.A.	21:39:26.76936	01:36:57	C03
decl.	+02:20:22.6968	09:33:47	C03
$\mu\alpha \cos \delta$ (mas yr ⁻¹)	485.9 ± 2.0	1238.982 ± 1.189	C03, G18
$\mu\delta$ (mas yr ⁻¹)	124.8 ± 2.7	-17.353 ± 0.841	S13, G18
RV (km s ⁻¹)	-25.1 ± 0.3	12.3 ± 0.8	V17
Spectral Type (Opt/IR)	T2/T1.5	T2/T2.5	P16/B06, P16/A06
Parallax (mas)	96.5 ± 1.1	163.7 ± 0.7	Z21
Rotation Period (hr)	7.619 ± 0.0168	2.414 ± 0.078	Y16
$v \sin i$ (km s ⁻¹)	18.7 ± 0.3	$52.8_{-1.1}^{+1.0}$	V17
Photometry			
2MASS J (mag)	15.264 ± 0.049	13.455 ± 0.030	C03
Fundamental Parameters from SED Analysis			
L_{bol}	-4.84 ± 0.02	-4.65 ± 0.06	This work
T_{eff} (K)	1040 ± 60	1150 ± 70	This work
Radius (R_{Jup})	1.14 ± 0.11	1.15 ± 0.11	This work
Mass (M_{Jup})	16.2 ± 8.8	17.8 ± 11.9	This work
$\log g$	4.5 ± 0.4	4.5 ± 0.4	This work
Fundamental Parameters from Retrieval Analysis			
L_{bol}	-4.91 ± 0.005	-4.71 ± 0.002	This work
T_{eff} (K) ^a	1360 ± 20	1329 ± 17	This work
Radius (R_{Jup}) ^a	0.61 ± 0.02	0.81 ± 0.03	This work
Mass (M_{Jup}) ^a	2.82 ± 1.0	4.71 ± 0.8	This work
$\log g$	4.27 ± 0.2	4.25 ± 0.08	This work

Note.

^a We find that some of the fundamental parameters derived from our retrieval show poor consistency with the SED-derived values. We discuss these discrepancies in Section 8.1.

References: C03, Cutri et al. (2003); G18, Gaia Collaboration (2018); S13, Smart et al. (2013); V17, Vos et al. (2017); Y16, Yang et al. (2016); Z21, Zhang et al. (2021b); P16, Pineda et al. (2016); B06, Burgasser et al. (2006); A06, Artigau et al. (2006).

description of the retrieval framework, but summarize the key features and new additions below.

5.1. The Forward Model

Our radiative transfer scheme computes the emergent flux from a layered atmosphere in the two-stream source approximation (Toon et al. 1989) and includes scattering, as introduced by McKay et al. (1989) and adopted by numerous studies thereafter (e.g., Marley et al. 1996; Saumon & Marley 2008; Morley et al. 2012). We use a 64 layer atmosphere with geometric mean pressures in the range $\log P(\text{bar}) = -4$ – -2.3 , spaced in 0.1 dex intervals. The thermal

profile is parameterized following Madhusudhan & Seager (2009). This scheme describes the atmosphere in three zones:

$$\begin{aligned} P_0 < P < P_1: P &= P_0 e^{\alpha_1(T-T_0)^{\frac{1}{2}}} \quad (\text{Zone 1}); \\ P_1 < P < P_3: P &= P_2 e^{\alpha_2(T-T_2)^{\frac{1}{2}}} \quad (\text{Zone 2}); \\ P > P_3: T &= T_3 \quad (\text{Zone 3}), \end{aligned} \quad (1)$$

where P_0 and T_0 are the pressure and temperature at the top of the atmosphere, which becomes isothermal with temperature T_3 at pressure P_3 . P_0 is fixed by the atmospheric model, and parameters T_0 and T_1 can be eliminated due to continuity at the zonal boundaries. This leaves us with 6 free parameters: α_1 , α_2 , P_1 , P_2 , P_3 , and T_3 . Further ruling out a thermal inversion (i.e., setting $P_2 = P_1$) simplifies this to 5 parameters for our thermal profile: α_1 , α_2 , P_1 , P_3 , and T_3 .

5.2. Gas Opacities

We consider the following absorbing gases in our analysis: H_2O , CO , CO_2 , CH_4 , NH_3 , CrH , FeH , SiO , Na , and K . We chose to include these gases as they have been previously identified as important absorbing species in the spectra of L/T transition objects.

Layer optical depths due to absorbing gases are calculated using opacities sampled at $R = 10,000$, and are sourced from Freedman et al. (2008, 2014), with updated opacities described in Burningham et al. (2017). The line opacities are tabulated across our temperature–pressure range in 0.5 dex steps in pressure and 20–500 K steps in temperature across the 75–4000 K range. This is linearly interpolated to our working pressure grid.

We include continuum opacities for $\text{H}_2\text{--H}_2$ and $\text{H}_2\text{--He}$ collisionally induced absorption, using cross sections from Richard et al. (2012), Saumon et al. (2012). We also include Rayleigh scattering due to H_2 , He , and CH_4 , and continuum opacities due to bound-free and free-free absorption by H^- (Bell & Berrington 1987; John 1988) and free-free absorption by H_2^- (Bell 1980). We use Na and K alkali opacities from Burrows & Volobuyev (2003).

5.3. Gas Phase Abundances

We assume uniform-with-altitude mixing ratios for absorbing gases and constrain these abundances in the retrieval. This approach has been commonly used in retrievals (e.g., Burningham et al. 2017, 2021; Gonzales et al. 2020). While this simple assumption cuts down on the number of parameters in the retrieval, it will not capture variations of gas abundances with altitude, which may be important. Thermochemical equilibrium models predict that abundances of many of the key absorbers are expected to vary by several orders of magnitude within the 0.1–10 bar region from which we observe large contributions of flux (Burningham et al. 2021). In theory, retrievals of gas abundances that vary with altitude would be preferred; however the resulting large number of parameters produce a significant computational challenge. In an effort to address this issue, previous retrieval studies using the Brewster framework have tested models that assume chemical equilibrium, drawing gas fractions for each layer of the atmosphere from thermochemical equilibrium grids. However, these models have not been preferred over the uniform-with-altitude mixing ratios (Burningham et al. 2017, 2021; Gonzales et al. 2020), and we do not adopt these models in this work.

5.4. Cloud Model

Our cloud model is made up of three components—(1) the location and structure of the cloud, (2) the optical properties of the cloud particles that define its opacity as a function of wavelength, and (3) the existence of *patches*.

5.4.1. Location and Structure of the Cloud

The vertical cloud structure can be described using two options—a *deck* or *slab* cloud. Each structure is defined by how the cloud opacity varies with pressure. The *deck* cloud is the simpler of the two models, and is an optically thick cloud where only the top of the cloud is visible. The deck cloud is parameterized by the pressure at which its total optical depth at $1 \mu\text{m}$ passes unity, P_{deck} , and a decay height, $\Delta \log P$, over which the optical depth decreases at shallower pressures and increases at deeper pressures as described in Burningham et al. (2021), Gonzales et al. (2020). Deck clouds can become opaque rapidly with increasing pressure, such that minimal atmospheric information from below the deck cloud is accessible. This is important to keep in mind when interpreting retrieval results—for the atmospheric retrieval models containing a deck cloud, the profile below the deck cloud simply extends the gradient of the profile at the cloud deck.

The *slab* cloud differs from the deck in that this cloud is not forced to become optically thick at some pressure. Thus, along with the parameters that it shares with the deck cloud (P_{deck} , $\Delta \log P$), the slab parameters also include the total optical depth at $1 \mu\text{m}$, τ_{cloud} . The optical depth is distributed through its extent as $d\tau/dP \propto P$, and reaches its total value at the high-pressure extent of the slab. We restrict the prior of the optical depth to the range 0–100.

5.4.2. Optical Properties of the Cloud Particles

We consider the wavelength-dependent optical properties of different condensate species under the assumption of Mie scattering. We source optical data for condensates from a variety of studies described in Burningham et al. (2021) and have pre-tabulated Mie coefficients as a function of radius and wavelength. We calculate the wavelength optical depths, single scattering albedos, and phase angles in each layer within the retrieval by integrating cross sections and Mie efficiencies over the particle size distribution in that layer for each condensate species. The total particle number density for a given condensate in each layer is calibrated to the optical depth at $1 \mu\text{m}$ as calculated by the parameterized cloud model. In this work, we only test retrieval models that assume a Hansen (1971) distribution of particle sizes, because the previous retrieval studies reported in Burningham et al. (2017), Burningham et al. (2021) find that this particle size distribution provided better retrieved fits for cloudy brown dwarf spectra.

5.4.3. Patchy Cloud Model

In this paper, we introduce a patchy cloud model to the Brewster retrieval framework. As our two targets are known to exhibit consistent, high-amplitude variability and are thus likely to have heterogeneous atmospheres, SIMP J0136+09 and 2MASS J2139+02 are the ideal targets to test this parameterization. Within Brewster, patches are represented by individual atmospheric columns over which the radiative transfer is calculated. The flux from each column is then

combined linearly according to their covering fractions to give the total emergent spectrum:

$$F_{\text{total}} = CF_{(P1)} + (1 - C)F_{(P2)}, \quad (2)$$

where F_{total} is the total flux, $F_{(P1)}$ is the flux from patch (1), $F_{(P2)}$ is the flux from patch (2), and C is the covering fraction. Within the Brewster retrieval framework, each patch can contain 0–2 different cloud structures. Only the cloud properties differ between columns—the gas abundances and pressure-temperature profile remains the same between columns.

5.5. The Retrieval Model

The retrieval process consists of optimizing the parameters of the forward model such that the resultant spectrum provides the best match to the observed spectrum. As described by Burningham et al. (2017), we use a Bayesian framework to optimize the model fit to the data by varying the input parameters.

Bayes' theorem provides a method to calculate the probability of a set of parameters (x) given the data (y), called the posterior probability:

$$p(x|y) = \frac{\mathcal{L}(y|x)p(x)}{p(y)}, \quad (3)$$

where \mathcal{L} is the likelihood of the data given the model parameters, $p(x)$ is the prior probability on the parameter set, and $p(y)$ is the probability of the data marginalized over all parameter values. When using the above equation for parameter estimation, the denominator acts as a normalization factor, so to map out the posterior probability distribution $p(x|y)$, we only consider the two terms that make up the numerator.

We use the EMCEE affine-invariant implementation of the Markov Chain Monte Carlo method (Foreman-Mackey et al. 2013) to sample the posterior probability distribution. We use a log-likelihood function to assess the fit of the data to the model:

$$\ln \mathcal{L}(y|x) = -\frac{1}{2} \sum_{i=1}^n \frac{(y_i - F_i(x))^2}{s_i^2} - \frac{1}{2} \ln(2\pi s_i^2), \quad (4)$$

where y_i corresponds to the observed spectral flux points $i = 0 \dots n$, s_i corresponds to the error on each flux point, and F_i is the forward model flux points for the current set of parameters, x . As described in Burningham et al. (2017), our errors are inflated using a tolerance parameter to allow for unaccounted sources of uncertainty.

5.6. Model Selection

We rank our models according to the Bayesian Information Criterion (BIC) in order of increasing ΔBIC from the best-fit model. The BIC is defined as

$$\text{BIC} = -2 \ln \mathcal{L}_{\text{max}} + k \ln N, \quad (5)$$

where \mathcal{L}_{max} is the maximum likelihood achievable by the model, k is the number of parameters in the model, and N is the number of data points used in the fit (Schwarz 1978).

The model with the lowest BIC is the preferred model, and we follow the significance thresholds of Kass & Raftery (1995) for model preference:

1. $0 < \Delta\text{BIC} < 2$, no preference worth mentioning;
2. $2 < \Delta\text{BIC} < 6$, positive preference;

Table 2

List of Models Tested in This Work for SIMP J0136+09 and 2MASS J2139+02 along with ΔBIC

Model	N Params	SIMP J0136	2MASS J2139
		+09 ΔBIC	+02 ΔBIC
Patchy Forsterite Slab and Iron Deck	32	0	0
Forsterite Slab and Iron Deck	31	118	8
Enstatite Slab and Iron Deck	31	119	10
Patchy Enstatite Slab and Iron Deck	32	77	19
Forsterite Slab	27	105	20
Iron Deck	26	104	38
Enstatite Slab	27	140	52
Forsterite Deck	26	123	56
No Clouds	22	578	56
Enstatite Deck	26	131	59
Iron Slab	26	120	65

Note. Models are arranged in order of the most favored model to least favored model for 2MASS J2139+02.

3. $6 < \Delta\text{BIC} < 10$, strong preference;
4. $10 < \Delta\text{BIC}$, very strong preference.

A variety of cloud parameterizations were explored for 2MASS J2139+02 and SIMP J0136+09. Following the strategies from previous retrieval studies (Burningham et al. 2017, 2021), we start with the simplest model available—a cloud-free model—and increase the complexity until we arrive at our best-fit model for each target. Our model choices are driven by the phase-equilibrium chemistry and cloud modeling predictions of expected species (e.g., Burrows et al. 2001; Lodders & Fegley 2002; Helling et al. 2008; Visscher et al. 2010) as well as the past detections of particular species in the literature (e.g., Cushing et al. 2006; Burningham et al. 2021; Luna & Morley 2021).

6. SIMP J0136+09 Retrieval Results

We show the list of models tested for SIMP J0136+09 with the number of parameters and ΔBIC for each model in Table 2. The top-ranked model for SIMP J0136+09 is comprised of a patchy forsterite (Mg_2SiO_4) slab lying above a deep, iron (Fe) deck cloud. Out of the models we tested, the second best model has a $\Delta\text{BIC} = 39$, indicating that the patchy forsterite slab and iron deck model is very strongly preferred by the data. In Table 3 we show the retrieved gas abundances and surface gravity for the winning model.

Figure 1 shows the model spectrum for the median set of parameters for the top-ranked model compared to the input data. The retrieved model reproduces the shape of the spectrum from 1 to 15 μm . In Figure 1, we also show self-consistent models from the Sonora Diamondback models (C. Morley et al. 2022, in preparation), which are an extension of the Sonora grid models (Karalidi et al. 2021; Marley et al. 2021) to cloudy atmospheres. The models shown have $T_{\text{eff}} = 1100$ K, $\log g = 4.25$, and sedimentation efficiency, $f_{\text{sed}} = 1-3$. The f_{sed} parameter, originating from the Ackerman & Marley (2001) cloud model, controls the efficiency with which cloud particles settle out of the cloud. The smaller f_{sed} values correspond to

Table 3

Summary of Retrieved Gas Abundances for the Preferred Models for SIMP J0136+09 and 2MASS J2139+02

	SIMP J0136+09	2MASS J2139+02
H ₂ O	$-4.03^{+0.03}_{-0.03}$	$-3.84^{+0.07}_{-0.06}$
CO	$-3.60^{+0.06}_{-0.06}$	$-3.24^{+0.10}_{-0.09}$
CO ₂	$-7.00^{+0.06}_{-0.07}$	$-4.87^{+0.15}_{-0.74}$
CH ₄	$-4.64^{+0.05}_{-0.04}$	$-4.65^{+0.10}_{-0.09}$
NH ₃	$-6.09^{+0.12}_{-0.13}$	$-5.64^{+0.15}_{-0.13}$
CrH	$-9.75^{+0.12}_{-0.13}$	$-9.47^{+0.16}_{-0.16}$
FeH	$-9.33^{+0.06}_{-0.06}$	$-9.68^{+0.14}_{-0.18}$
SiO	$-9.09^{+1.95}_{-1.97}$	$-9.55^{+2.02}_{-1.59}$
Na+K	$-6.39^{+0.08}_{-0.08}$	$-6.51^{+0.15}_{-0.15}$
log(<i>g</i>)	$4.25^{+0.08}_{-0.08}$	$4.27^{+0.16}_{-0.13}$

lower sedimentation efficiency, which results in vertically extended clouds that are composed of smaller particles. Larger f_{sed} values correspond to efficient sedimentation, which leads to physically thinner clouds composed of larger particles. The Sonora models capture the shape of the dominant absorbers but struggle to reproduce the overall shape of the spectrum. This is due to the lack of flexibility of the forward model compared to our retrieved model.

6.1. Thermal Profile

Figure 2 shows the retrieved thermal profile and cloud pressures for the winning SIMP J0136+09 model compared with self-consistent grid models and phase-equilibrium condensation curves and the Sonora Diamondback models. The models shown have $T_{\text{eff}} = 1100$ K, $\log g = 4.25$, and sedimentation efficiency, $f_{\text{sed}} = 1-3$. Models with $f_{\text{sed}} = 2-3$ generally agree with the retrieved profile at all pressures probed, with the exception of the $\sim 0.1-1$ bar region in which the model profiles are $>3\sigma$ hotter. This discrepancy highlights the advantages of using a flexible retrieval model to constrain atmospheric parameters and also the opportunity of using atmospheric retrieval results to inform future directions for forward models. The forward models solve for radiative-convective equilibrium given assumed elemental abundances and cloud properties. The physical processes underlying the departure of the retrieved profile from the forward model remain a topic of future investigation. The $f_{\text{sed}} = 1$ model provides a poorer match to the retrieved profile, but it is notable that the detached radiative zone in the model profile (visible as the kink in the pressure-temperature profile at ~ 1600 K) approximately coincides with the pressure location of our retrieved forsterite slab cloud. Such detached radiative zones are driven by the formation of atmospheric clouds (Tsuji 2002; Burrows et al. 2006), so their overlap in pressure space indicates that the retrieved cloud pressure level is consistent with the forward model.

6.2. Cloud Properties

The preferred model is comprised of a patchy forsterite slab cloud and a deeper iron deck cloud. A summary of the retrieved parameters for the preferred models is presented in Table 4. The top-ranked model is a relatively complicated one that consists of two types of clouds, one of which is patchy. This model complexity is enabled by our large wavelength range, as was also found by Burningham et al. (2021) who found a

similarly complex best-fit model for 2MASS 2224-01 using this wavelength range.

The median pressures of these clouds are indicated by the shaded regions in the right-hand panels of Figure 2. The forsterite slab cloud is the highest altitude cloud in the model, with a cloud base pressure of $\log P(\text{bar}) = 0.24^{+0.06}_{-0.05}$ dex. Both its height and depth are well constrained by the retrieval. The iron deck is located deeper than the forsterite slab, with a well-constrained $\tau_{\text{Fe}} = 1$ pressure level, of $\log P(\text{bar}) = 0.90^{+0.04}_{-0.05}$ dex. The pressure change over which the optical depth of the iron clouds drops from 1.0 to 0.5 is constrained to $d\log P = 0.06^{+0.03}_{-0.02}$. This represents a cloud with a small decay height, which is confined to a narrow range of pressures. This cloud is notably different to the iron deck retrieved for the L dwarf 2M2224-01 by Burningham et al. (2021), whose iron deck cloud has a similar $\tau_{\text{Fe}} = 1$ pressure level, but with a much larger scale height. This is likely driven by the lower temperatures of the T2 type SIMP J0136+09, which results in the formation of iron clouds at deeper pressures.

Figure 2 also shows the condensation curves for several species, calculated for solar composition gas following (Visscher et al. 2010). Condensation curves provide a useful guide on the species that can condense in the atmosphere, but do not indicate whether that particular condensate will necessarily form. The pressure depths of both retrieved clouds are consistent with being located to the left of their respective condensation curves on the retrieved thermal profile—they are both located at cooler temperatures and shallower pressures than the condensation point and are thus consistent with condensation chemistry predictions.

As discussed in Section 5.4, our models use Mie scattering clouds with a Hansen distribution for particle sizes. For SIMP J0136+09, we find that both cloud species are dominated by submicron-sized grains with a negligible number of particles larger than $1 \mu\text{m}$.

Our top-ranked model is one that contains two *patches*, as discussed in Section 5.4. Patch (1) consists of the forsterite slab cloud and an iron deck cloud, while patch (2) consists of the deeper iron deck cloud. This parameterization adds only one additional parameter to the model—the covering fraction of patch (1). Our retrieval constrains the coverage of patch (1) to $70^{+3}_{-4}\%$ of the surface. The top ranking of a cloud model consisting of multiple patches supports the idea of an inhomogeneous atmosphere, as first concluded from time-resolved variability monitoring (Artigau et al. 2009; Apai et al. 2013). We will discuss the implications of this patchy model in Section 8.2.

6.3. Bulk Properties

Figure A1 shows the posterior distributions for the retrieved gas fractions and $\log g$, along with derived values for radius, mass, atmospheric metallicity, and C/O ratio, and extrapolated T_{eff} . We also present these values in Table 1. The radius is estimated using the retrieved model scaling factor and Gaia parallax. The mass is then computed using the derived radius and the retrieved $\log g$. L_{bol} is found by extrapolating the retrieved model to cover the $0.5-20 \mu\text{m}$ range, summing the flux, and scaling by $4\pi D^2$, where D is the distance. T_{eff} is then determined using the extrapolated L_{bol} and inferred radius. The atmospheric C/O ratio is estimated under the assumption that all carbon and oxygen in the atmosphere exist within the

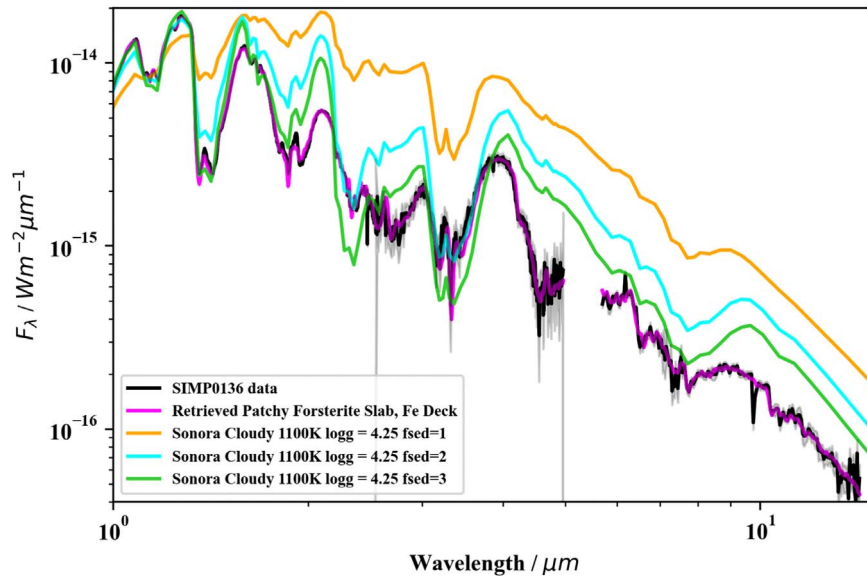


Figure 1. Maximum likelihood retrieved model spectrum (pink) for the top-ranked model for SIMP J0136+09 overlaid with the data (black). Self-consistent grid models are shown for comparison, and are scaled to match the J -band flux in the observed spectrum.

absorbing gases included in the retrieval. The metallicity is estimated by considering elements within our retrieved absorbing gases and comparing their inferred abundances to their solar values (Asplund et al. 2009).

We find that some of the fundamental parameters derived from our retrieval show poor consistency with the SED-derived values. We discuss these discrepancies in more detail in Section 8.1.

7. 2MASS J2139+02 Retrieval Results

Table 2 shows the list of models tested for 2MASS J2139+02 along with the number of parameters for each model and the resulting ΔBIC . The winning model for 2MASS J2139+02 consists of a patchy forsterite slab cloud and an iron deck cloud—the very same model that is preferred for our twin object SIMP J0136+09. With a $\Delta\text{BIC} = 8$ between the winning and second best model, the patchy forsterite slab and iron deck model is very strongly preferred over all of the models tested.

In Figure 3, we show the top-ranked model spectral fit along with the observed spectrum. The retrieved model spectrum fits the entire 1–15 μm spectral range very well. We also show the Sonora Diamondback models in Figure 3. Similarly to the spectral fit presented for SIMP J0136+09 in Section 6, the retrieval provides a better fit to the overall spectrum due to the flexibility of the model.

7.1. Thermal Profile

Figure 4 shows the retrieved thermal profile and cloud pressure for the winning model compared to self-consistent grid models and phase-equilibrium condensation curves. As in Figure 2, we show Sonora Diamondback models as comparison (C. Morley et al. 2022, in preparation), and show the $T_{\text{eff}} = 1100$ K, $\log g = 4.25$, and sedimentation efficiency, $f_{\text{sed}} = 1$ –3. The $f_{\text{sed}} = 2$ –3 models show good agreement with our retrieved thermal profile below 0.3 bar; however our retrieved profile is slightly warmer than both models at shallower pressures.

7.2. Cloud Properties

The spectrum of 2MASS J2139+02 is best described by a patchy forsterite slab cloud and an iron deck cloud. We present a summary of the cloud parameters for 2MASS J2139+02 in Table 4.

The pressures of the two cloud species in the atmosphere of 2MASS J2139+02 are shown by the shaded regions to the right of Figure 4. The forsterite slab lies at a shallower pressure in the atmosphere, with a well-constrained base pressure of $\log P = 0.12^{+0.08}_{-0.09}$ dex, and a height of $d \log P = 0.32^{+0.20}_{-0.15}$ dex. The coverage of the patchy forsterite slab cloud is constrained to $83\% \pm 6\%$ of the surface. These parameters are very similar to those retrieved for SIMP J0136+09.

The iron cloud deck becomes optically thick at deeper pressures of ~ 7 bar. The location of the $\tau_{\text{Fe}} = 1.0$ pressure level is tightly constrained to $\log P$ (bar) = $0.86^{+0.09}_{-0.07}$ dex. The median value for the pressure over which the optical depth drops from $\tau_{\text{Fe}} = 1.0$ to $\tau_{\text{Fe}} = 0.5$ is small ($d \log P = 0.03$), which indicates a compact cloud that is confined to deeper pressures.

Figure 4 also shows the condensation curves for several species of interest, as discussed in Section 6.2. The forsterite slab cloud is placed at pressures and temperatures consistent with those expected from forsterite condensation curves. The $\tau_{\text{Fe}} = 1.0$ pressure level for the iron deck cloud lies approximately at the intersection of the pressure-temperature (P/T) profile and the Fe condensation curve, and its pressure location is thus consistent with condensation curve chemistry.

All of the models we tested used Mie scattering and Hansen particle distributions. For 2MASS J2139+02, the slab cloud is dominated by submicron-sized particles (median size $\sim 0.06 \mu\text{m}$), with a negligible number of particles larger than $1 \mu\text{m}$. The deck cloud is also composed of submicron particles (median size $\sim 0.05 \mu\text{m}$).

7.3. Bulk Properties

Figure A2 shows the posterior distributions for the retrieved gas fractions for absorbing gases and $\log g$ for our winning

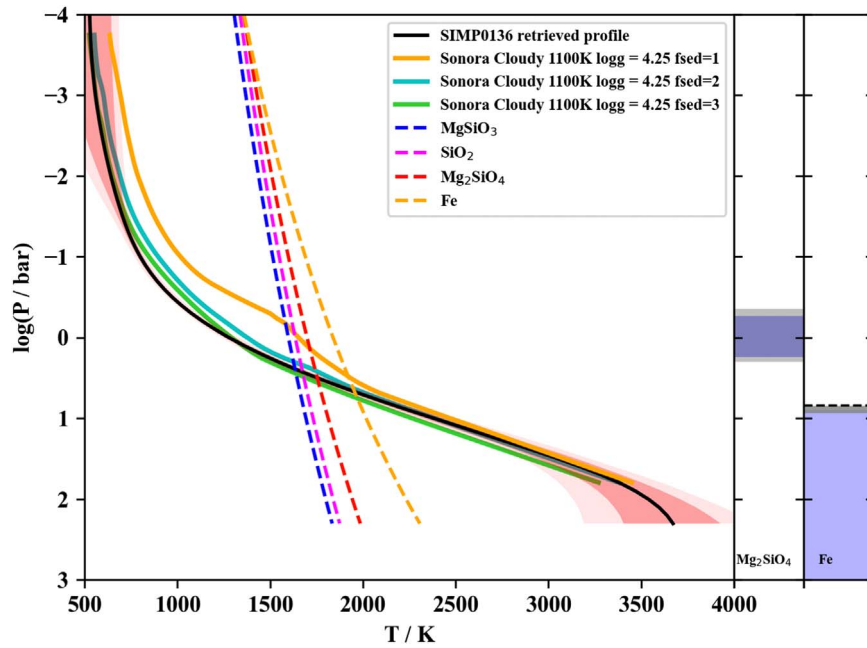


Figure 2. Retrieved thermal profile (black line, pink shading for 1σ and 2σ intervals) and cloud pressures for SIMP J0136+09. Self-consistent model profiles from the Sonora Diamondback (C. Morley et al. 2022, in preparation) grid are plotted as solid colored lines. Phase-equilibrium condensation curves for possible condensate species are plotted as colored dashed lines. The cloud pressures for the forsterite (Mg_2SiO_4) slab and the iron (Fe) deck are indicated in bars to the left of the P/T profile. Purple shading indicates the median cloud location for the cloud, with gray shading indicating the 1σ range.

model for 2MASS J2139+02. We derive values for radius, mass, atmospheric metallicity, C/O ratio, and T_{eff} using the method discussed in Section 6.3. These values are also given in Table 1.

As in the case of SIMP J0136+09, we find that the retrieved and SED-derived values are generally inconsistent with each other, with the exception of L_{bol} and $\log g$. These discrepancies are discussed in detail in Section 8.1.

7.4. Discrepant Feature in the Spectrum of 2MASS J2139+02

While the retrieved spectral fit for 2MASS J2139+02 (Figure 3) provides a good overall fit, it is clear that the best-fit retrieval fails to adequately fit the 7–10 μm region. In fact, none of the models tested on this spectrum provided a good fit in this part of the spectrum—all models underestimate the flux in this region.

Our first assumption was that this may be due to an overestimation of the abundance of one of our absorbing gases within the model. This could arise due to our assumed vertically constant abundances whereby a good fit in one part of the spectrum may force a poor fit in another part of the spectrum if the abundance of an absorbing gas changes rapidly through the atmosphere. However, having compared the spectral contributions of each of our absorbing gases, we find that none of these gases uniquely coincide with this region. We conclude that the discrepancies between the observed and retrieved spectra are not caused by an overestimation of the abundances of the gases within our model.

We also consider whether systematics may cause the feature in the spectrum. In particular, the overlap region between the first and second Short-Low modes (SL2 and SL1) (7.4–8.7 μm) approximately corresponds to the region of discrepancy between the data and model. To combine the spectra from each mode, Suárez & Metchev (2022) use SL1 spectra at wavelengths $>7.5 \mu\text{m}$. Having obtained both SL1 and SL2

mode spectra (G. Suarez, priv. comm.) and compared the spectra in the overlap region, we find that the spectra agree across modes, indicating that this feature is likely not caused by a stitching error.

For the purposes of this work, the most important question is whether this region is driving our model ranking or the parameters within our best-fit model. To answer this, we performed a smaller set of retrievals on a spectrum of 2MASS J2139+02 with the 7–10 μm region removed. We show the resulting ΔBIC values for these runs in Table 5. The patchy forsterite and iron deck model is still the highest ranking model when this wavelength region is removed, and the retrieved parameters are consistent across both models.

8. Discussion

8.1. Comparison with SED-derived Fundamental Parameters

We find consistency between our extrapolated and retrieved L_{bol} and $\log g$ values and the SED-derived values (shown in Table 1). In both cases, the retrieval L_{bol} value is slightly higher than the SED value, but falls within the range expected from past retrieval studies (Gonzales et al. 2020, 2022; Calamari et al. 2022). We also find that our retrieved and SED-derived $\log g$ values are consistent.

Our derived radii for 2MASS J2139+02 and SIMP J0136+09 are considerably smaller than the evolutionary models’ predictions. Relatedly, our high derived T_{eff} values are driven by the small retrieved radius. The low derived masses are also likely caused by the small retrieved radius. The retrieved $\log g$ is driven by the impact of the scale height of the atmosphere on spectral features, and is found to be consistent with evolutionary model predictions. However, when combined with the small radius, it implies a very low mass that is inconsistent with evolutionary model predictions.

There are many instances in the literature of studies that retrieve unexpectedly small radii, particularly in the mid L to

Table 4
Summary of Retrieved Cloud Properties for the Preferred Models for SIMP J0136+09 and 2MASS J2139+02

	SIMP J0136+09		2MASS J2139+02	
Cloud No.	1	2	1	2
Type	Slab	Deck	Slab	Deck
Species	Mg ₂ SiO ₄	Fe	Mg ₂ SiO ₄	Fe
Cloud Coverage	0.70 ^{+0.03} _{-0.04}	n/a	0.83 ^{+0.06} _{-0.06}	n/a
Max τ_{cloud} at 1 μm	12.03 ^{+1.03} _{-0.85}	n/a	8.17 ^{+1.54} _{-1.38}	n/a
Reference Pressure/ $\log P$ (bar)	0.24 ^{+0.06} _{-0.05} (max τ)	0.90 ^{+0.04} _{-0.05} ($\tau = 1$)	0.12 ^{+0.08} _{-0.09} (max τ)	0.86 ^{+0.09} _{-0.07} ($\tau = 1$)
Height/ $d\log P$ (bar)	0.50 ^{+0.09} _{-0.096}	0.06 ^{+0.03} _{-0.02}	0.32 ^{+0.20} _{-0.15}	0.03 ^{+0.03} _{-0.02}
Log (effective particle radius $a/\mu\text{m}$)	-1.47 ^{+0.14} _{-0.14}	-1.35 ^{+0.25} _{-0.31}	-1.21 ^{+0.18} _{-0.19}	-1.31 ^{+0.45} _{-0.66}
Particle Radius Spread (Hansen distribution b)	0.36 ^{+0.33} _{-0.25}	0.51 ^{+0.33} _{-0.33}	0.42 ^{+0.34} _{-0.29}	0.52 ^{+0.34} _{-0.35}

early T spectral type regime. Using the Brewster retrieval framework, Burningham et al. (2021) found a similarly small radius for the cloudy L dwarf 2MASS 2224–01, the only other object retrieved with a similar wavelength range. Small radii have also been found for L and L/T transition dwarfs using other retrieval frameworks (e.g., Kitzmann et al. 2020; Mollière et al. 2020; Lueber et al. 2022; Zhang et al. 2021a) and self-consistent modeling frameworks (e.g., Barman et al. 2011; Sorahana et al. 2013; Brock et al. 2021). Additionally, Zalesky et al. (2019) report anomalously small radii for a sample of late-T and early Y dwarfs. In contrast, the retrieved radii for mid type T dwarfs are generally consistent with evolutionary models (e.g., Line et al. 2017; Gonzales et al. 2020; Calamari et al. 2022). The prevalence of this problem for the objects with temperatures where clouds are thought to be abundant in the atmosphere suggests that the problem may be linked to the existence of clouds. As discussed by Burningham et al. (2021), the existence of a gray cloud at very shallow pressures would act to reduce the total flux and thus allow the radius to increase. However, such a cloud would require much larger particle sizes than those that have been retrieved in this or other retrieval studies in order to produce a primarily gray opacity.

8.2. Patchy Forsterite Clouds for Two Variable Planetary-mass Objects

The winning models for SIMP J0136+09 and 2MASS J2139+02 are strikingly similar; the preferred models consist of a patchy forsterite slab cloud above an iron deck in each case. Since our parameterization of cloud opacity does not incorporate cloud condensation models to determine which clouds are favored, it is encouraging that the retrieved presence of forsterite is also predicted by a range of microphysical and phase-equilibrium models at solar composition (e.g., Helling et al. 2006; Lodders & Fegley 2006; Visscher et al. 2010; Gao et al. 2020). While this model is very strongly preferred by the data for both targets, the ΔBIC values are more decisive for SIMP J0136+09 across all models (see Table 2). This is primarily due to the inclusion of the AKARI/IRC spectrum for SIMP J0136+09, which provides more data points to assess each model, and secondarily due to the higher S/N of the spectra for SIMP J0136+09 (see Section 3 for a discussion of the spectra and their S/N).

The results presented here demonstrate for the first time that a patchy model has been preferred within a retrieval framework. The fact that both targets are photometrically and spectroscopically variable (e.g., Artigau et al. 2009; Radigan et al. 2012; Apai et al. 2013) provides independent evidence for the heterogeneous nature of their atmospheres, and was thus

one of our main motivators for testing a patchy cloud model to reproduce their spectra.

Beyond the fact that the same model is preferred for both of our targets, the properties of the retrieved clouds are very similar for both SIMP J0136+09 and 2MASS J2139+02. We show the cloud properties for the preferred model for each object in Table 4. In both cases, the patchy forsterite cloud has a similar level of coverage (70% for SIMP J0136+09 and 83% for 2MASS J2139+02). The forsterite clouds are situated at similar pressures of 1.3–1.7 bar, and have similar heights (2–5 bar). The optical depth of SIMP J0136+09’s forsterite cloud is marginally larger. The forsterite slab for both objects is comprised of submicron particles of radius 0.03–0.06 μm with a negligible number of particles with radii above 1 μm . Similarly, the properties of the iron deck cloud are consistent across both targets—the deck cloud in both cases is situated at 7–8 bar and is composed of submicron-sized grains.

We show the contribution functions for each model in Figure 5. The contribution function in an atmospheric layer that lies between pressures P_1 and P_2 is defined as

$$C(\lambda, P) = \frac{B(\lambda, T(P)) \int_{P_1}^{P_2} d\tau}{\exp \int_0^{P_2} d\tau}, \quad (6)$$

where $B(\lambda, T(P))$ is the Planck function. Since a patchy model is preferred for both 2MASS J2139+02 and SIMP J0136+09, we obtain two contribution functions for each object. Patch (1) consists of the forsterite slab and an iron deck while patch (2) consists of solely the iron deck cloud. As we expect from the similarity between the retrieved parameters for both targets, the contribution functions for 2MASS J2139+02 and SIMP J0136+09 are remarkably similar. In patch (1), we see that the forsterite slab contributes to the flux at ~ 1 –2, ~ 4 , and ~ 9 –11 μm for both models, with the gas opacity contributing flux in other wavelength regions. In patch (2), we note a contribution of the iron deck in a small wavelength range shortward of $\sim 1.5 \mu\text{m}$, with the gas opacity dominating elsewhere.

8.3. Linking the Observed Variability Signatures to Brewster Retrieval Results

A major goal of this work is to link our retrieval results with the observed spectral variability signatures previously reported in the literature for our targets, specifically the HST/WFC3 monitoring observation presented by Apai et al. (2013; and discussed in detail in Section 2). Based on the observed spectral

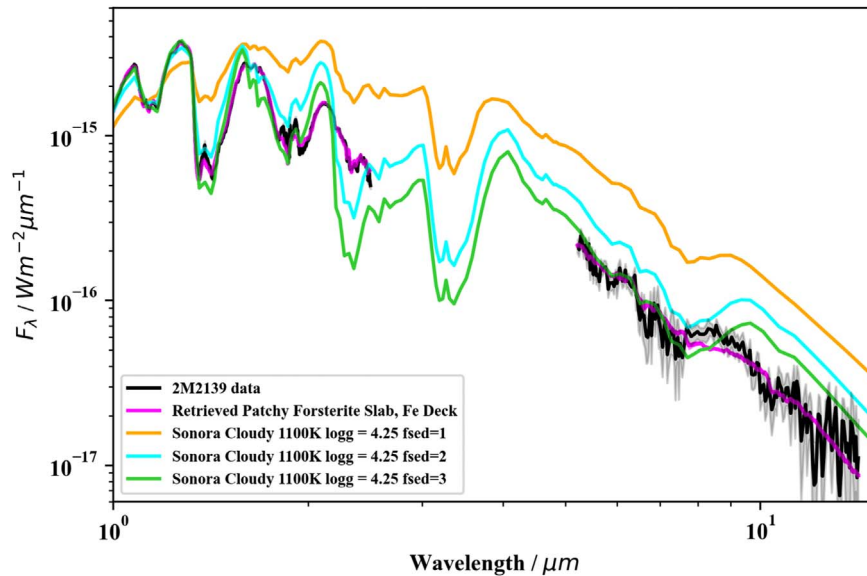


Figure 3. Maximum likelihood retrieved model spectrum (pink) for the top-ranked model for 2MASS J2139+02 overlaid with the data (black). Self-consistent grid models are shown for comparison, and are scaled to match the J -band flux in the observed spectrum.

variability, the authors used the color information to provide a picture of the atmospheric cloud structures responsible for the observed variability. They conclude that the spectral behavior of both targets is best described by a heterogeneous mixture of high-altitude, cool, thick clouds and deeper, hotter, thin clouds. In this section, we investigate whether the observed variability could be explained using our top-ranked model.

Using the contribution functions presented in Figure 5, we can begin to approximate the variability that may be caused by the patchy forsterite slab cloud. We determine the photosphere of each patch as the pressure at which we reach $\tau = 1$ due to either cloud or gas opacity. We then calculate ΔP as the difference in pressures and ΔT as the difference in temperatures of the photosphere between the two patches. ΔP and ΔT are thus a measurement of how much deeper and hotter we observe into the atmosphere in patch (2) (consisting of the iron deck cloud only) compared to that in patch (1) (consisting of the forsterite slab and the iron deck clouds). In Figure 6, we show the change in pressure (top) and temperature (bottom) between patch (1) and patch (2) for both targets. Since we find very similar cloud structures for SIMP J0136+09 and 2MASS J2139+02, it is not surprising that the changes in pressure and temperature are very similar. The temperature changes are larger for SIMP J0136+09 due to a slightly steeper slope in the P/T profile at the pressures between cloud layers (shown in Figure 2).

The large ΔT values between the photosphere of each patch are notable. If the variability were driven by a single region defined by patch (1), with a temperature that is 200–1200 K cooler than the second region defined by patch (2), one would expect an amplitude much larger than that observed for either object. We argue that these results imply that the regions that define patch (1) are distributed mostly homogeneous as opposed to forming one large region in the atmosphere. To achieve the variability amplitudes that have been measured for SIMP J0136+09 and 2MASS J2139+02, the heterogeneity in the silicate cloud cover must represent a small fraction of the total silicate cloud covering fractions that we have retrieved for

our targets. We investigate this idea in more detail in the following analyses.

We also find that the spectral behavior of ΔP and ΔT broadly matches the shape of the observed variability: the highest variability amplitude occurs at $\sim 1.25 \mu\text{m}$, where ΔP and ΔT are the highest, while the lowest variability amplitude is observed in the water band at $\sim 1.4 \mu\text{m}$ where ΔP and ΔT are at their lowest. This broad agreement in shape suggests that the variability may be driven by the patchy forsterite cloud.

To investigate this possibility directly, we estimate the spectral variability driven by a patchy forsterite cloud within our retrieved model by comparing the spectra from each patch. Additionally, we can use the observed HST/WFC3 variability reported by Apai et al. (2013) to estimate how the variability is related to the coverage fraction for each object—a large change in the silicate cloud coverage will naturally lead to higher amplitudes and vice versa. Treating our retrieved silicate cloud coverage percentages (shown in Table 4) as the average silicate coverage for each target, we experimented with different silicate coverage changes until the retrieved variability signatures matched the observed values in the HST/WFC3 wavelength region of 1.1–1.7 μm , and show our results in Figure 7. Using this technique, we find that, for 2MASS J2139+02, we can approximately reproduce the observed variability with a silicate cloud coverage percentage change of 16%. Assuming that the silicate cloud coverage constrained by our retrieval represents the average coverage percentage, our analysis predicts that the silicate cloud coverage changes from 75%–91% to reproduce the observed variability. For SIMP J0136+09, we can reproduce the observed variability amplitude with a silicate cloud coverage percentage change of 3%. Taking our retrieved coverage as the average value, we find that the silicate cloud coverage percentage likely changes from 69% to 72%. Our results suggest that a greater change in silicate cloud coverage drives the larger variability amplitude observed in 2MASS J2139+02 compared to that of SIMP J0136+09.

A number of studies have suggested a link between the rotation rate and the size of cloud structures in extrasolar

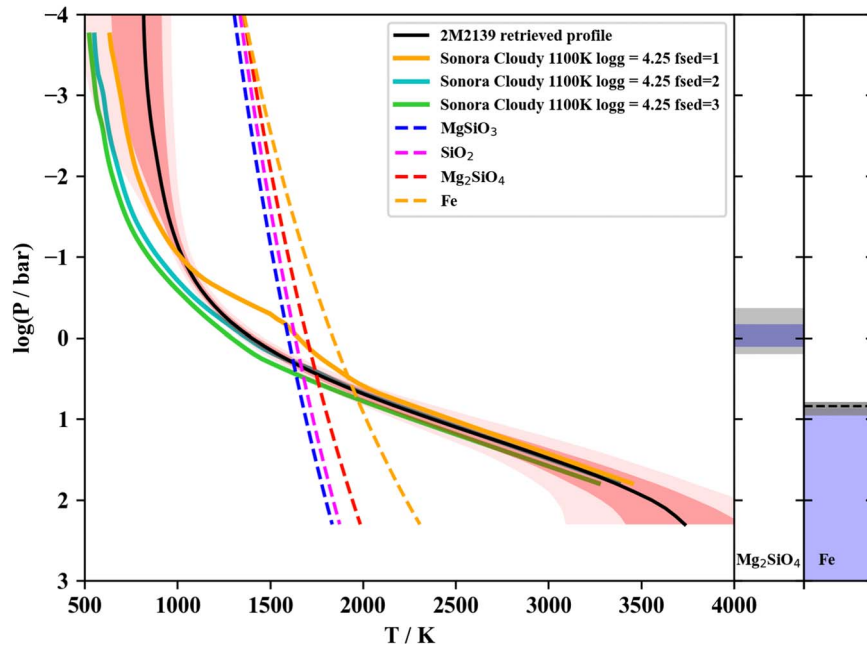


Figure 4. Retrieved thermal profile (black line, pink shading for 1σ and 2σ intervals) and cloud pressures for 2MASS J2139+02. Self-consistent model profiles from the Sonora Diamondback (C. Morley et al. 2022, in preparation) grid are plotted as solid colored lines. Phase-equilibrium condensation curves for possible condensate species are plotted as colored dashed lines. The cloud pressures for the forsterite (Mg_2SiO_4) slab and the iron (Fe) deck are indicated in bars to the left of the P/T profile. Purple shading indicates the median cloud location for the cloud, with gray shading indicating the 1σ range.

Table 5

Models Tested in This Work for the 2MASS J2139+02 Spectrum without the 7–10 μm Region with Their Corresponding ΔBIC Values

Model	N Params	ΔBIC
No Clouds	20	280
Forsterite Slab and Iron Deck	29	8
Patchy Forsterite Slab and Iron Deck	32	0
Patchy Enstatite Slab and Iron Deck	32	42

Note. The patchy forsterite and iron deck model is still the highest ranking model when this wavelength region is removed.

atmospheres. These results represent an excellent test case for this potential link. The atmospheric circulation models presented by Tan & Showman (2021) show that the atmospheres of giant exoplanet and brown dwarfs are likely to be dominated by cloud-forming and clear-sky vortices that are seen to evolve with time. The study highlights the importance of the Rossby deformation radius in setting the maximum size of storms and vortices. The Rossby deformation radius is inversely proportional to the local rotational rate when other parameters are the same. In the case of SIMP J0136+09 and 2MASS J2139+02, our retrieval results have shown that their atmospheres are almost identical. Thus, any differences in the cloud structure may be driven by rotation rate. With a rotation period of 7.6 hr, the deformation radius of 2MASS J2139+02 would be larger than that of SIMP J0136+09, whose rotation period is 2.4 hr. This would result in larger cloud-forming and clear-sky vortices emerging for 2MASS J2139+02, which would naturally result in larger variability amplitudes as these large-scale structures rotate in and out of view. The results presented in this work strongly support this interpretation. Since the cloud layers for SIMP J0136+09 and 2MASS J2139+02 are at almost identical pressure levels, the changes in pressure and temperature achieved by seeing to pressures

deeper than the forsterite slab are also very similar (i.e., see Figure 6). This means that greater contrasts between the forsterite and iron cloud layers do not drive greater amplitudes for 2MASS J2139+02. Instead, it seems that larger atmospheric features are responsible for the large amplitudes in 2MASS J2139+02.

We find that the variability predicted by our retrieval—i.e., changes in brightness driven by the patchy forsterite slab cloud—broadly matches the behavior of the HST/WFC3 results. While the retrieval does not perfectly match the observed variability, it is expected that the variability behavior may have changed slightly between the HST/WFC3 observations and the epochs of our spectra. Moreover, the results shown in Figure 7 also predict significant variability in the Spitzer [3.6 μm] and [4.5 μm] bands, such as those reported by Yang et al. (2016). We show the noncontemporaneous Spitzer variability amplitudes reported by Yang et al. (2016) in Figure 7, but do not use these values to scale our retrieval prediction. These variability amplitudes are consistent with the predicted amplitudes from our retrieval for SIMP J0136+09, but are higher than the amplitude predicted for 2MASS J2139+02 in Spitzer channel (2) ([4.5 μm]). The light curves of SIMP J0136+09 and 2MASS J2139+02 reported by Yang et al. (2016) show significant light-curve evolution, and hence a large range in amplitudes that is reflected in Figure 7. This shows the importance of simultaneous variability monitoring in order to investigate extrasolar atmospheres in detail.

Finally, our retrieval model predicts significant variability at 10 μm that is driven by the silicate scattering feature. Although multiple studies have speculated that variability is likely present at this feature (e.g., Luna & Morley 2021), variability monitoring at these wavelengths has not been possible until now. JWST/MIRI will provide the means to monitor this region closely in order to identify silicate clouds as the driver of variability.

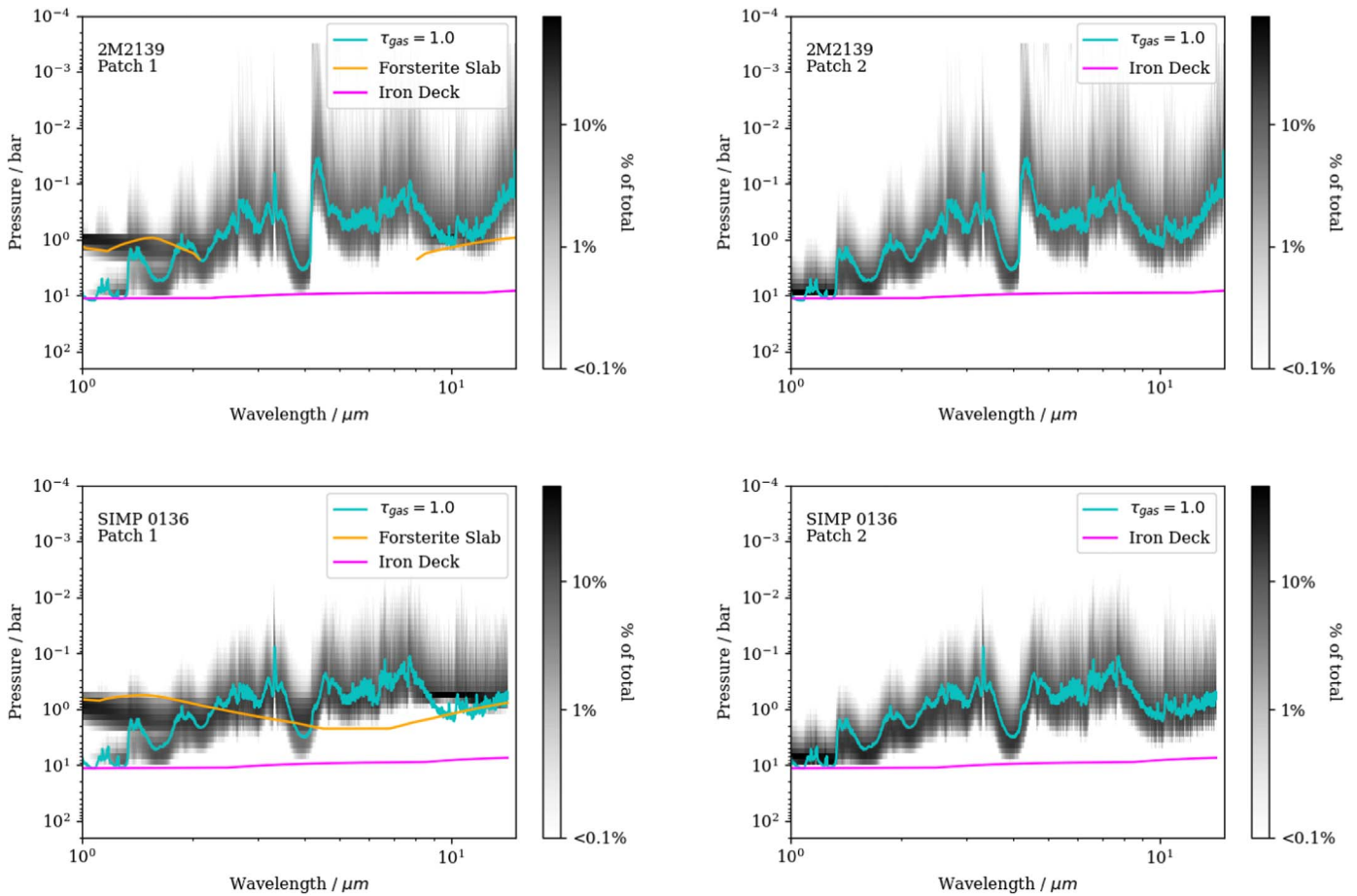


Figure 5. Contribution functions for 2MASS J2139+02 (top) and SIMP J0136+09 (bottom) based on the maximum likelihood retrieved parameters for the top-ranked model in each case. We show separate contribution functions for patch (1) (forsterite slab above an iron deck, left) and patch (2) (iron deck, right). The black shading shows the percentage contribution of each pressure to the flux at each wavelength. $\tau = 1$ lines are included for gas phase opacities (cyan), the forsterite slab (orange), and the iron deck (pink). For 2MASS J2139+02, the forsterite slab cloud does not become optically thick at wavelengths of $\sim 2\text{--}8\ \mu\text{m}$, so there is a break in this line.

This broad agreement is promising, but there remain some details that that retrieval results do not explain. In particular, using simultaneous variability monitoring with HST and Spitzer, Yang et al. (2016) report a phase shift of 30° between the near-IR and mid-IR light curves and a correlation between these measured phase shifts and the pressure levels probed by each wavelength. Such behavior is likely driven by complex vertical behavior, such as vertically varying cloud structures or P/T profile variations above the clouds that are not captured by our one-dimensional patchy cloud framework.

8.4. C/O Ratio among Two Carina-near Members

The chemical composition of extrasolar atmospheres is often considered the key to disentangling the formation pathways of stars, brown dwarfs, and planets. In particular, a large number of studies have targeted the C/O ratio in an attempt to reveal the formation mechanism of exoplanets (Öberg et al. 2011; Madhusudhan 2012); however it is likely to be difficult to tease out a direct link between the measured C/O and formation mechanism (Mollière et al. 2022). Measuring C/O ratios in benchmark systems is thus critical for understanding and calibrating this measurement.

SIMP J0136+09 and 2MASS J2139+02 are both members of the 200 Myr Carina-Near moving group and therefore are expected to have formed in the same molecular cloud,

alongside other stars, brown dwarfs, and planetary-mass objects. With similar masses, we would also expect similar subsequent evolution. To the first order, we would thus expect their C/O ratios to be consistent with each other, and with the larger sample of Carina-Near brown dwarfs and stars.

Numerous studies have highlighted the difference between the *atmospheric* C/O ratio and the *intrinsic* C/O ratio (Line et al. 2015; Calamari et al. 2022; Mollière et al. 2022). *Atmospheric* C/O ratios can be measured to high precision using atmospheric retrievals (e.g., Zalesky et al. 2019; Calamari et al. 2022); however how they relate to the *intrinsic* values is an open question. Cloud condensation processes, such as the formation of a forsterite cloud found in this work, can deplete the atmospheric oxygen or other species, resulting in atmospheric C/O ratios that differ from their intrinsic values. Within our standard retrieval framework, we estimate the atmospheric C/O ratio for our targets by assuming that all carbon and oxygen are contained in the considered absorbing gases. We find consistent C/O ratios in our targets (see corner plots in Figures A1 and A2)—measuring $C/O = 0.79 \pm 0.02$ for SIMP J0136+09, and $C/O = 0.82 \pm 0.03$ for 2MASS J2139+02. Their agreement is in line with our first-order expectations that these two worlds formed from the same starting material, proceeded on a similar evolutionary pathway, and have very similar atmospheres.

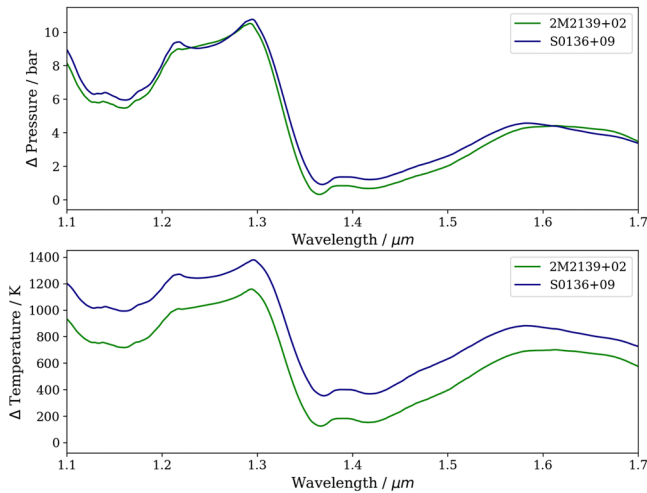


Figure 6. The change in pressure, ΔP , (top) and the change in temperature, ΔT , (bottom) for 2MASS J2139+02 (blue) and SIMP J0136+09 (purple) between patch (1) (iron deck and forsterite slab) and patch (2) (iron deck only). We determine the photosphere of each patch as the pressure at which we reach $\tau = 1$ due to either cloud or gas opacity. We then calculate ΔP as the difference in pressures and ΔT as the difference in temperatures between the photospheres of the two patches of our model. ΔP and ΔT are thus a measurement of how much deeper and hotter we observe into the atmosphere in patch (2) compared to patch (1). The high ΔT values suggest that much of the coverage for patch (1) is distributed homogeneously. The shape of both ΔT and ΔP as a function of wavelength broadly matches the shape of the observed variability reported by Apai et al. (2013).

While their atmospheric C/O ratios are in agreement, it is challenging to estimate the intrinsic or bulk C/O ratios. Our C/O estimate does not include any oxygen contained in condensates such as Mg_2SiO_4 , which we have detected in the atmospheres of our targets. Atmospheric retrieval studies in the literature have typically applied corrections to account for such oxygen depletion. Burrows & Sharp (1999) estimate that 3.28 oxygen atoms are removed from the gas phase for every silicon atom under the assumption that enstatite, (MgSiO_3) is the dominant condensation species with forsterite (Mg_2SiO_4) as a secondary species. Since we find that forsterite is the dominant condensate in the atmospheres of SIMP J0136+09 and 2MASS J2139+02, this would result in the depletion of up to 4 oxygen atoms per silicon atom. Taking this into account, we estimate that the *intrinsic* C/O ratio could be as low as 0.56 for SIMP J0136+09 and 0.59 for 2MASS J2139+02, values more in line with stellar C/O ratios reported in the literature (Nissen 2013, 2015; Brewer & Fischer 2016).

If we assume that both SIMP J0136+09 and 2MASS J2139+02 formed like stars, we would expect that their intrinsic C/O ratios match those of their stellar counterparts in the Carina-Near moving group. Measurements of stellar and brown dwarf C/O ratios across well-characterized young moving groups such as Carina-Near would thus be an opportunity to gain a greater understanding of the relationship between atmospheric and intrinsic C/O ratios in cloudy worlds.

8.5. Differences in Chemistry

We present our retrieved gas abundances in Table 3. The retrieved gas abundances show perhaps the greatest differences between SIMP J0136+09 and 2MASS J2139+02. Of particular interest are the lower abundances retrieved for H_2O and CO for SIMP J0136+09 as these are some of the most abundant gases found for 2MASS J2139+02 and are

significantly different in our two targets. These lower abundances are responsible for the low metallicity that we derive for SIMP J0136+09. These differences may be due to our data quality and/or retrieval methodology, or may have an astrophysical explanation. We will briefly touch on these possibilities in this section.

As discussed in Section 3, the available data for SIMP J0136+09 and 2MASS J2139+02 are quite different. In particular, for SIMP J0136+09, the combination of SpeX, AKARI, and Spitzer/IRS data provides us with complete wavelength coverage from 1 to 15 μm , while for 2MASS J2139+02 we are missing the 2.5–5 μm region. This means that we achieve more complete coverage of the pressure levels within the atmosphere for SIMP J0136+09. To test whether these discrepancies were caused by the inclusion of the AKARI data for SIMP J0136+09, we ran our highest ranked model on only the SpeX and Spitzer/IRS portions of the spectrum, and found that the retrieved gas abundances (along with the other retrieved parameters) were consistent with and without this portion of the spectrum. From this we conclude that the inclusion of the 2.5–5 μm spectrum does not affect the measured abundances in this case, and does not cause the low metallicity derived for SIMP J0136+09.

As discussed in Section 3, the SpeX spectra for both targets are of similar quality, with average S/N ranging from 167–180. The S/N of the Spitzer/IRS spectrum of 2MASS J2139+02 is significantly lower than that of SIMP J0136+09 (average S/N of 5 versus 15). S/N differences are unlikely to cause the lower measured abundances of H_2O and CO in SIMP J0136+09 because our data for this target is of higher S/N, thus making it easier to detect such gases in the spectra.

Another possibility is that our retrieval framework may be responsible for the differing abundance measurements. The Brewster retrieval framework uses vertically constant mixing ratios to describe each gas within the model. In Figure 8, we show our retrieved gas mixing ratios along with predictions from thermochemical equilibrium models interpolated for our derived metallicity and C/O ratio. The thermochemical equilibrium models predict that many of the included gases will vary substantially as a function of altitude within the pressure levels probed by our spectra (e.g., FeH, CrH), while others are predicted to remain relatively constant with altitude. Our gases of interest, H_2O and CO, are not predicted to change significantly, but it is possible that, by failing to capture the behavior of gases that do change substantially, this could have an indirect effect on the retrieved abundances of H_2O and CO. However, we expect that this would affect the retrieved abundances for both targets in the same way, so our assumption of vertically constant mixing ratios cannot be the underlying cause for these changes. Rather, it is likely that there are differences in either the data (as discussed previously) or astrophysical differences (discussed next) that are revealed by these differing abundance measurements.

There are a number of astrophysical processes that may drive these differing abundances. The first major difference between our targets is that SIMP J0136+09 has been shown to be an auroral emitter (Kao et al. 2016) while there is no evidence in the literature that 2MASS J2139+02 emits aurorae.

Auroral activity in brown dwarfs is of the same nature as the auroral emission produced by the giant planets in our own solar system and is driven by strong-field-aligned currents that drive accelerated electron beams. These accelerated electrons can

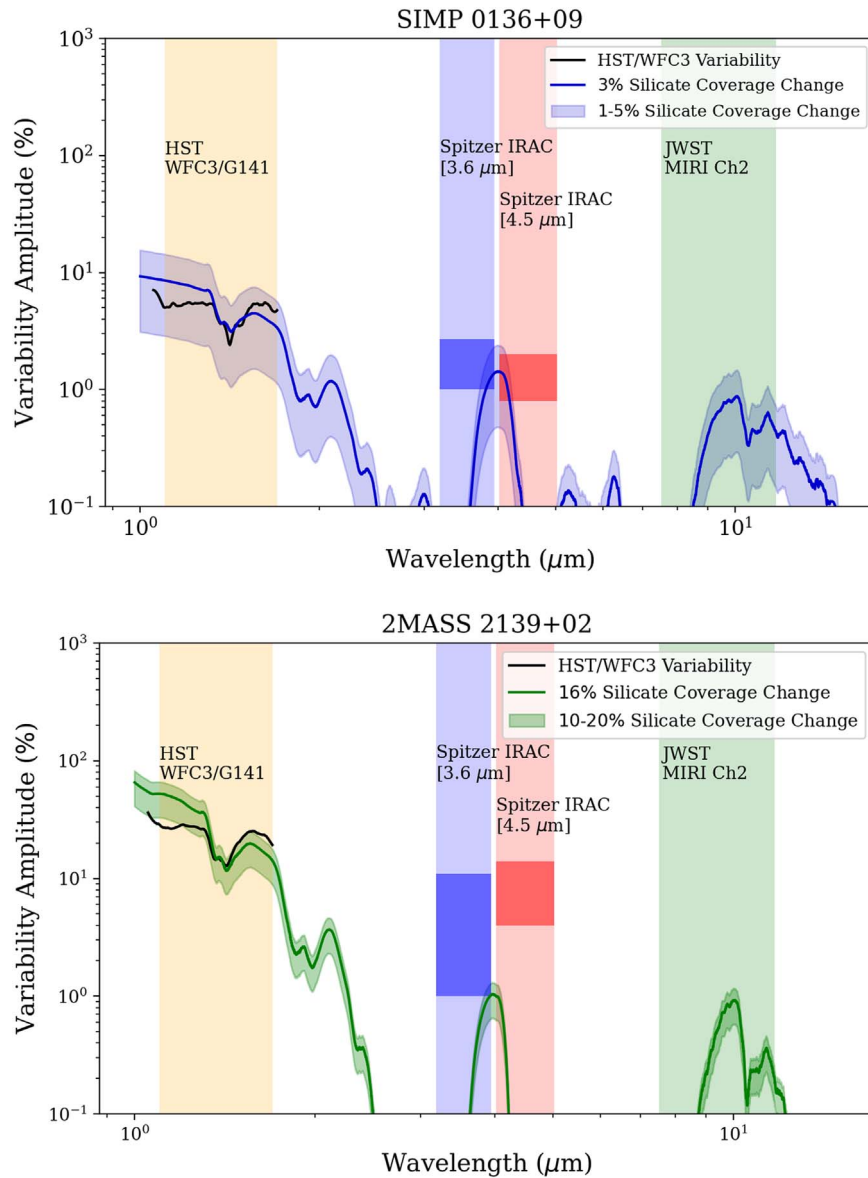


Figure 7. Comparison of our retrieval results with the observed spectral variability reported by Apai et al. (2013) for SIMP J0136+09 (top) and 2MASS J2139+02 (bottom). The predicted spectral variability driven by our retrieved patchy forsterite cloud slab is shown by the blue line for SIMP J0136+09 and green line for 2MASS J2139+02. The range of amplitudes that would be predicted for a range of other silicate coverage changes is also shown by the semitransparent blue and green shading for context. The observed spectral variability from Apai et al. (2013) is shown in black. The darker blue and red regions within Spitzer/IRAC channels (1) and (2) show the range of amplitudes reported for SIMP J0136+09 and 2MASS J2139+02 by Yang et al. (2016) during noncontemporaneous observations. The predicted variability signatures from our retrieved model broadly match the observed HST/WFC3 grism spectral variability and predict lower amplitudes in the Spitzer 3.6 and 4.5 μm bands. Our retrieval also suggests that significant spectral variability will be observed in the silicate feature at $\sim 10 \mu\text{m}$ (accessible by JWST) due to the patchy forsterite slab.

lead to the onset of the electron cyclotron maser instability that produces detectable radio emission (e.g., Hallinan et al. 2015; Kao et al. 2016, 2018; Pineda et al. 2017; Allers et al. 2020; Richey-Yowell et al. 2020). These energetic electron beams may also have a significant effect on the atmosphere. In Jupiter and Saturn, the collisions between electrons and the atmospheric gases lead to optical and UV emissions due to excitation and ionization processes, and the subsequent ion chemistry leads to the formation of strongly emitting H_3^+ (Perry et al. 1999; Vasavada et al. 1999) ions. It is likely that the auroral activity in the atmospheres of brown dwarfs also leads to the formation of detectable amounts of H_3^+ , but this has not yet been observed (Pineda et al. 2017; Gibbs & Fitzgerald 2022). In this work, we can speculate on whether the auroral

activity on SIMP J0136+09 could lead to the suppression of H_2O and CO absorption.

One possibility is that the presence of auroral currents leads to the destruction of H_2O and CO . Interestingly, Helling & Rimmer (2019) provide such a mechanism. Using three-dimensional simulations that include kinetic cloud formation and kinetic ion-neutral chemistry, the authors model the atmospheric chemistry of the brown dwarf auroral emitter LSR-1835 to study the formation and evolution of H_3^+ . These simulations show that, for the case of LSR-1835, small amounts of H_3^+ ions can form at pressures down to ~ 0.1 bar, but that H_3^+ reacts rapidly with H_2O and CO , and can produce the relatively stable ion hydronium, H_3O^+ , at pressures down to ~ 1 bar. Gibbs & Fitzgerald (2022) recently provided upper

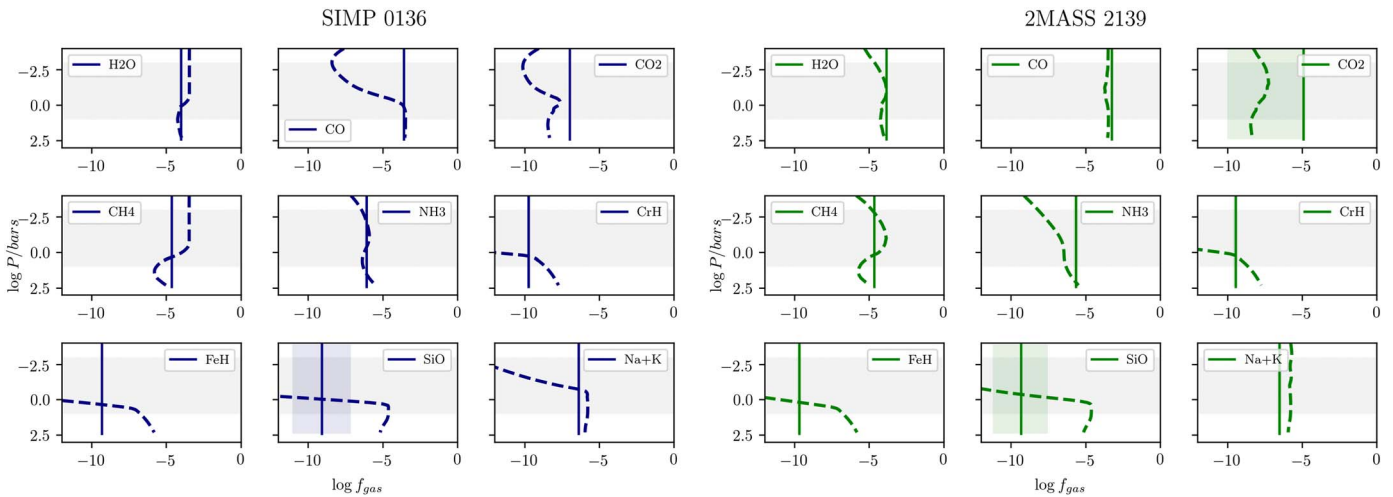


Figure 8. Retrieved gas fractions compared to predictions from thermochemical grids for SIMP J0136+09 (left) and 2MASS J2139+02 (right). Equilibrium predictions are shown as dashed lines and are calculated for our estimated $[M/H]$ and C/O values. The solid straight lines and shading show hour median retrieved values and 16th to 84th percentiles, respectively.

limits on the abundances of H_3^+ in the atmosphere of SIMP J0136+09, suggesting that this ion may indeed be short-lived in the atmosphere. Whether the reactions of H_2O and CO with H_3^+ could account for their significantly depleted abundances in SIMP J0136+09 will be an interesting future investigation.

A second major difference is the differing rotation periods of our targets—2.4 hr for SIMP J0136+09 and 7.6 hr for 2MASS J2139+02. Atmospheric dynamical simulations presented by Tan & Showman (2021) highlight the importance of the rotation rate on regulating the atmospheres of brown dwarfs and giant planets. One of their conclusions is that faster rotation tends to weaken the vertical transport of vapor and clouds, which may have a measurable effect on retrieved abundances of various species. However, it is hard to explain the relative depletion of H_2O and CO in SIMP J0136+09 with this mechanism while other important and abundant gases such as CH_4 remain consistent between SIMP J0136+09 and 2MASS J2139+02. In-depth atmospheric dynamical simulations of SIMP J0136+09 and 2MASS J2139+02 are needed to fully explore the influence of the rotation period on the abundances of atmospheric gases.

Finally, there is likely to be some intrinsic atmospheric diversity among extrasolar atmospheres. Carrying out detailed retrieval studies on a larger sample of objects will reveal the range of atmospheric parameters that we can expect from otherwise similar extrasolar worlds.

8.6. Atmospheric Retrievals in the Era of JWST

Retrievals of extrasolar atmospheres utilizing high precision spectra with wide wavelength ranges of 1–20 μm will soon be commonplace in the era of JWST (e.g., Miles et al. 2022). The results of this work, alongside the previously published retrieval study of 2MASS 2224–01 by Burningham et al. (2021), which both make use of Spitzer/IRS data to achieve a wavelength range of 1–15 μm , highlight the detail in which we can characterize an atmosphere with such data. Both studies found that the data were best described by a complex cloud structure—slabs containing enstatite and quartz along with an iron deck for 2MASS 2224–01 and a patchy forsterite slab with an iron deck for both SIMP J0136+09 and 2MASS J2139+02.

Since JWST will provide spectra of higher resolution and higher signal-to-noise, which are acquired near-simultaneously, the retrievals of these data will likely reveal the atmospheres of these worlds in even more detail and accuracy than we have presented here.

Additionally, JWST will allow us to extend our spectroscopic monitoring efforts beyond the HST/WFC3 grism wavelength range of 1.1–1.7 μm , and to provide a wealth of information on how wavelengths beyond 2 μm change over time. Spectroscopic variability studies at a wider wavelength range will reveal the time-resolved behavior of these atmospheres at a broader range of pressures than before. Of particular interest will be the behavior of the 10 μm silicate feature (e.g., Luna & Morley 2021; Figure 7 of this work). The spectroscopic variability monitoring with JWST may even enable longitudinally resolved retrievals for brown dwarfs and planetary-mass objects, as has recently been carried out for hot Jupiters (e.g., Cubillos et al. 2021; MacDonald & Lewis 2022; Nixon & Madhusudhan 2022). The work presented here represents a good starting point for future retrieval studies using wide wavelength coverage provided by JWST.

9. Summary and Conclusions

In this work, we present an atmospheric retrieval analysis of 1–15 μm spectra of the isolated exoplanet analogs SIMP J0136+09 and 2MASS J2139+02 using the Brewster retrieval framework. These targets are an interesting pair of objects to study, because they share their ages, masses, temperatures, and variability properties with each other.

We test a number of different models and find that the spectra of SIMP J0136+09 and 2MASS J2139+02 are best described by a model containing a patchy forsterite slab cloud lying above an iron deck cloud. The properties of the clouds are strikingly similar between our two targets. Both atmospheres contain a patchy forsterite slab whose cloud base is located at a pressure of 1.3–1.7 bar that is composed of submicron grains and an iron deck that is located at a pressure of ~ 7 bar that is also composed of submicron-sized grains. We constrain the covering fractions for the forsterite clouds to be ~ 0.7 for SIMP J0136+09 and ~ 0.8 for 2MASS J2139+02.

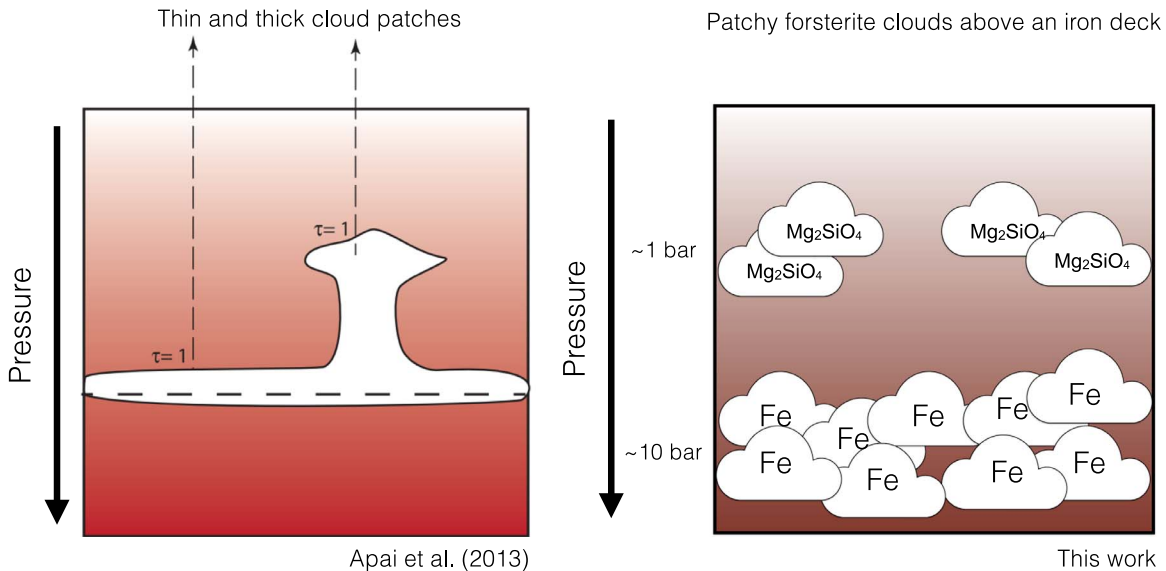


Figure 9. Illustrations proposed by Apai et al. (2013; left) and this work (right) for the atmospheric structure of SIMP J0136+09 and 2MASS J2139+02. Apai et al. (2013) find that a cloud deck of varying thickness could explain their observed HST/WFC3 variability observations. Our atmospheric retrieval analysis of a single 1–15 μm spectrum provides a similar, but more detailed view into the atmospheres of SIMP J0136+09 and 2MASS J2139+02.

Both SIMP J0136+09 and 2MASS J2139+02 are known to exhibit large amplitude spectroscopic variability (Artigau et al. 2009; Radigan et al. 2012; Apai et al. 2013), which has generally been interpreted as arising from inhomogeneous clouds rotating in and out of view. The preference of our retrieval analysis for models that contain patchy clouds provides independent support for inhomogeneous clouds in the atmospheres of our targets. We investigate whether our retrieved model atmosphere is consistent with the spectroscopic variability observations presented by Apai et al. (2013) and find that the spectral behavior of the variability broadly matches the predicted variability that we can derive from our retrieval. We find that the amplitude of variability can be reproduced if the silicate cloud coverage changes from 69%–72% for SIMP J0136+09 and 75%–91% for 2MASS J2139+02. This work suggests that the larger variability amplitudes observed for 2MASS J2139+02 are driven by larger atmospheric features that form as a result of its larger Rossby deformation radius. Our retrieved atmospheric model also predicts significant variability in the [3.6 μm] and [4.5 μm] Spitzer bands (as has been observed by Yang et al. 2016) and across the 10 μm scattering feature, which can be probed with JWST/MIRI.

In Figure 9, we provide a comparison that summarizes the atmospheric structure presented by Apai et al. (2013; left) and in this work (right). Based on HST/WFC3 spectroscopic variability observations, Apai et al. (2013) proposed that the atmosphere consists of a cloud of varying thickness, with regions composed of hotter, thinner clouds and regions of cooler, thicker clouds. Using a spectrum for each object from 1 to 15 μm , the work presented in this study clarifies this view significantly. Our retrieval analysis finds evidence for two distinct cloud layers, the top cloud composed of patchy forsterite slab clouds and the bottom cloud composed of a thick iron deck. We have also constrained the pressure of each cloud layer as well as the particle sizes for each cloud species.

We find consistent atmospheric C/O ratios of 0.79 ± 0.02 dex for SIMP J0136+09, and 0.82 ± 0.03 dex for

2MASS J2139+02, which is expected given that they are both members of the Carina-Near moving group with very similar atmospheres. Estimating their intrinsic C/O ratios is challenging because of oxygen depletion due to forsterite clouds forming in the atmosphere, but we estimate intrinsic C/O ratios as low as 0.56 for SIMP J0136+09 and 0.59 for 2MASS J2139+02, which are closer to expectations for stars of similar ages.

We find slightly different abundances of H_2O and CO in our targets, which may be due to the data quality, retrieval framework, and/or astrophysical processes such as auroral activity or atmospheric dynamics driven by their different rotation periods. As we build upon the sample of brown dwarfs with in-depth atmospheric retrievals, these differences can be placed in context, and the aforementioned possibilities can be investigated in more detail.

Finally, we believe that the results presented here represent an encouraging preliminary study for the types of investigations that will become possible as observations of brown dwarfs and giant exoplanets at wavelengths of 1–20 μm become commonplace in the era of JWST [e.g., see the first such JWST observation presented in the literature Miles et al. 2022]. The results shown in this work highlight the power of such wavelength ranges for characterizing extrasolar atmospheres in exceptional detail. As these current and upcoming JWST observations will be of higher signal-to-noise, of higher resolution, and taken near-simultaneously, future retrieval studies that make use of these data should provide an even clearer view of extrasolar atmospheres than the one presented in this work.

We thank the anonymous referee for useful comments, which improved the quality of this work. The data used in this publication were collected through the MENDEL high-performance computing (HPC) cluster at the American Museum of Natural History. This HPC cluster was developed with National Science Foundation (NSF) Campus Cyberinfrastructure support through Award #1925590. This work has made use of the University of Hertfordshire’s high-

performance computing facility. This work was supported by NSF Award 1909776, NASA XRP Award #80NSSC22K0142, and HST-GO-15924.001-A. E.G. acknowledges support from the Heising-Simons Foundation for this research. C.V.M. acknowledges support from NSF Astronomy and Astrophysics Research Grants grant No. 1910969. This work benefited from the 2022 Exoplanet Summer Program in the Other Worlds Laboratory (OWL) at the University of California, Santa Cruz, a program funded by the Heising-Simons Foundation.

Appendix Corner Plots

In Figures A1 and A2 we show the posterior distributions for retrieved and derived parameters in our winning models for both SIMP J0136+09 and 2MASS J2139+02. Posterior distributions of retrieved parameters for the other models we tested are provided at https://zenodo.org/record/7555471#.Y8r_AuzMIws.

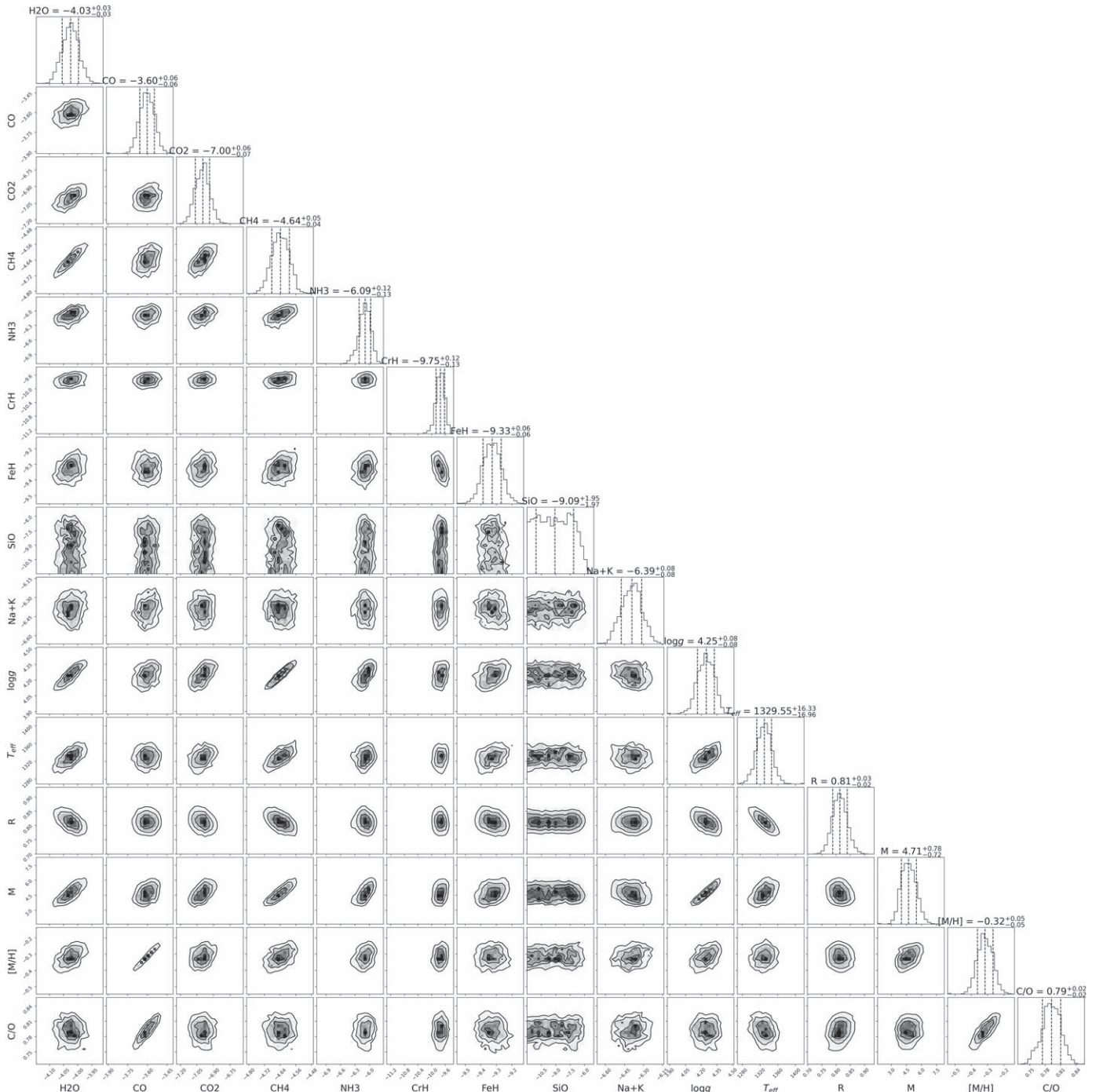


Figure A1. Corner plot showing the gas opacities, log g , and derived T_{eff} , R , M , $[M/H]$, and C/O ratio for the top-ranked model for SIMP J0136+09.

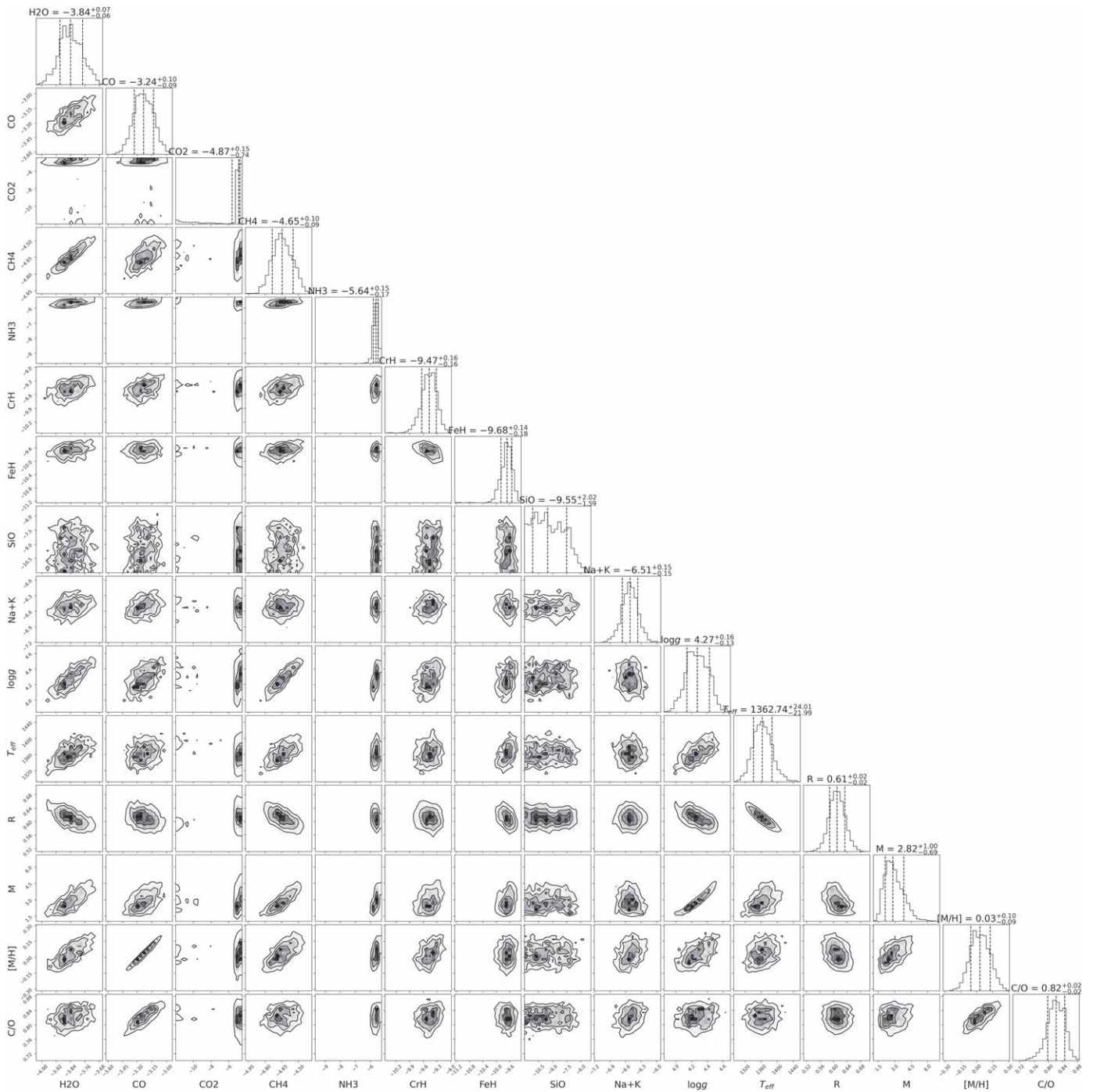


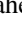
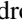


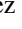
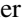

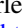





Figure A2. Corner plot showing the gas opacities, log g , and derived T_{eff} , R , M , $[M/H]$, and C/O ratio for the top-ranked model for 2MASS J2139+02.

ORCID iDs

Johanna M. Vos  <https://orcid.org/0000-0003-0489-1528>
 Ben Burningham  <https://orcid.org/0000-0003-4600-5627>
 Jacqueline K. Faherty  <https://orcid.org/0000-0001-6251-0573>
 Shereilyn Alejandro  <https://orcid.org/0000-0003-0548-0093>
 Eileen Gonzales  <https://orcid.org/0000-0003-4636-6676>
 Emily Calamari  <https://orcid.org/0000-0002-2682-0790>
 Daniella Bardalez Gagliuffi  <https://orcid.org/0000-0001-8170-7072>
 Channon Visscher  <https://orcid.org/0000-0001-6627-6067>
 Xianyu Tan  <https://orcid.org/0000-0003-2278-6932>
 Caroline V. Morley  <https://orcid.org/0000-0002-4404-0456>
 Mark Marley  <https://orcid.org/0000-0002-5251-2943>
 Marina E. Gemma  <https://orcid.org/0000-0002-8871-773X>
 Niall Whiteford  <https://orcid.org/0000-0001-8818-1544>

References

- Ackerman, A. S., & Marley, M. S. 2001, *ApJ*, **765**, 872
 Allard, F., Homeier, D., & Freytag, B. 2012, *RSPTA*, **370**, 2765
 Allers, K., Vos, J. M., Biller, B. A., & Williams, P. G. 2020, *Sci*, **368**, 169
 Apai, D., Karalidi, T., Marley, M. S., et al. 2017, *Sci*, **357**, 683
 Apai, D., Radigan, J., Buenzli, E., et al. 2013, *ApJ*, **768**, 121
 Artigau, É., Bouchard, S., Doyon, R., & Lafrenière, D. 2009, *ApJ*, **701**, 1534
 Artigau, É., Doyon, R., Lafrenière, D., et al. 2006, *ApJL*, **651**, L57
 Asplund, M., Grevesse, N., Sauval, A. J., & Scott, P. 2009, *ARA&A*, **47**, 481
 Barman, T. S., Macintosh, B., Konopacky, Q. M., & Marois, C. 2011, *ApJL*, **735**, L39
 Barstow, J. K., & Heng, K. 2020, *SSRv*, **216**, 82
 Bell, K. L. 1980, *JPhB*, **13**, 1859
 Bell, K. L., & Berrington, K. A. 1987, *MolPh*, **20**, 801
 Biller, B. A., Vos, J., Bonavita, M., et al. 2015, *ApJL*, **813**, L23
 Biller, B. A., Vos, J., Buenzli, E., et al. 2018, *AJ*, **155**, 95
 Bohn, A. J., Ginski, C., Kenworthy, M. A., et al. 2021, *A&A*, **648**, A73
 Bohn, A. J., Kenworthy, M. A., Ginski, C., et al. 2020, *ApJL*, **898**, L16
 Bowler, B. P., Zhou, Y., Morley, C. V., et al. 2020, *ApJL*, **893**, L30
 Brewer, J. M., & Fischer, D. A. 2016, *ApJ*, **831**, 20
 Brock, L., Barman, T., Konopacky, Q. M., & Stone, J. M. 2021, *ApJ*, **914**, 124
 Buenzli, E., Apai, D., Radigan, J., Reid, I. N., & Ffauvel, D. 2014, *ApJ*, **782**, 77
 Buenzli, E., Marley, M., Apai, D., et al. 2015, *ApJ*, **812**, 163
 Burgasser, A. J., Geballe, T. R., Leggett, S. K., Kirkpatrick, J. D., & Golimowski, D. A. 2006, *ApJ*, **637**, 1067
 Burgasser, A. J., Liu, M. C., Ireland, M. J., Cruz, K. L., & Dupuy, T. J. 2008, *ApJ*, **681**, 579
 Burningham, B., Faherty, J. K., Gonzales, E. C., et al. 2021, *MNRAS*, **506**, 1944
 Burningham, B., Marley, M. S., Line, M. R., et al. 2017, *MNRAS*, **470**, 1177
 Burrows, A., Hubbard, W. B., Lunine, J. I., & Liebert, J. 2001, *RvMP*, **73**, 719
 Burrows, A., & Sharp, C. M. 1999, *ApJ*, **512**, 843
 Burrows, A., Sudarsky, D., & Hubeny, I. 2006, *ApJ*, **640**, 1063
 Burrows, A., & Volobuyev, M. 2003, *ApJ*, **583**, 985
 Burrows, A., Marley, M., Hubbard, W. B., et al. 1997, *ApJ*, **491**, 856
 Calamari, E., Faherty, J. K., Burningham, B., et al. 2022, *ApJ*, **940**, 164
 Carter, A. L., Hinkley, S., Kammerer, J., et al. 2022, arXiv:2208.14990
 Chauvin, G., Lagrange, A.-M., Dumas, C., et al. 2004, *A&A*, **425**, L29
 Cubillos, P. E., Keating, D., Cowan, N. B., et al. 2021, *ApJ*, **915**, 45
 Cushing, M. C., Roellig, T. L., Marley, M. S., et al. 2006, *ApJ*, **648**, 614
 Cutri, R. M., Skrutskie, M. F., van Dyk, S., et al. 2003, *yCat*, **2246**, 0
 Faherty, J. K., Riedel, A. R., Cruz, K. L., et al. 2016, *ApJS*, **225**, 10
 Filippazzo, J. C., Rice, E. L., Faherty, J., et al. 2015, *ApJ*, **810**, 158
 Foreman-Mackey, D., Hogg, D. W., Lang, D., & Goodman, J. 2013, *PASP*, **125**, 306
 Freedman, R. S., Lustig-Yaeger, J., Fortney, J. J., et al. 2014, *ApJS*, **214**, 25
 Freedman, R. S., Marley, M. S., & Ladders, K. 2008, *ApJS*, **174**, 504
 Gagné, J., Faherty, J. K., Burgasser, A. J., et al. 2017, *ApJL*, **841**, L1
 Gaia Collaboration 2018, *yCat*, **1345**, 0
 Gao, P., Thøningren, D. P., Lee, G. K. H., et al. 2020, *NatAs*, **4**, 951
 Ge, H., Zhang, X., Fletcher, L. N., et al. 2019, *AJ*, **157**, 89
 Gelino, C., & Marley, M. 2000, in ASP Conf. Ser. 212, From Giant Planets to Cool Stars, ed. C. A. Griffith & M. S. Marley (San Francisco, CA: ASP), 322
 Gibbs, A., & Fitzgerald, M. P. 2022, *AJ*, **164**, 63
 Gonzales, E. C., Burningham, B., Faherty, J. K., et al. 2020, *ApJ*, **905**, 46
 Gonzales, E. C., Burningham, B., Faherty, J. K., et al. 2022, *ApJ*, **938**, 56
 Gonzales, E. C., Burningham, B., Faherty, J. K., et al. 2021, *ApJ*, **923**, 19
 Hallinan, G., Littlefair, S. P., Cotter, G., et al. 2015, *Natur*, **523**, 568
 Hansen, J. E. 1971, *JATs*, **28**, 1400
 Helling, C., & Rimmer, P. B. 2019, *RSPTA*, **377**, 20180398
 Helling, C., Ackerman, A., Allard, F., et al. 2008, *MNRAS*, **391**, 1854
 Helling, C., Thi, W. F., Woitke, P., & Fridlund, M. 2006, *A&A*, **451**, L9
 John, T. L. 1988, *A&A*, **193**, 189
 Kao, M. M., Hallinan, G., Pineda, J. S., Stevenson, D., & Burgasser, A. 2018, *ApJS*, **237**, 25
 Kao, M. M., Hallinan, G., Pineda, J. S., et al. 2016, *ApJ*, **818**, 24
 Karalidi, T., Marley, M., Fortney, J. J., et al. 2021, *ApJ*, **923**, 269
 Kass, R. E., & Raftery, A. E. 1995, *JASA*, **90**, 773
 Kitzmann, D., Heng, K., Oreshenko, M., et al. 2020, *ApJ*, **890**, 174
 Lagrange, A.-M., Bonnefoy, M., Chauvin, G., et al. 2010, *Sci*, **329**, 57
 Lee, J.-M., Fletcher, L. N., & Irwin, P. G. J. 2012, *MNRAS*, **420**, 170
 Lew, B. W. P., Apai, D., Zhou, Y., et al. 2016, *ApJL*, **829**, L32
 Line, M. R., Fortney, J. J., Marley, M. S., & Sorahana, S. 2014, *ApJ*, **793**, 33
 Line, M. R., Teske, J., Burningham, B., Fortney, J. J., & Marley, M. S. 2015, *ApJ*, **807**, 183
 Line, M. R., Marley, M. S., Liu, M. C., et al. 2017, *ApJ*, **848**, 83
 Liu, M. C., Dupuy, T. J., & Allers, K. N. 2016, *ApJ*, **833**, 96
 Ladders, K., & Fegley, B. 2002, *Icar*, **155**, 393
 Ladders, K., & Fegley, B. J. 2006, in *Astrophysics Update 2*, ed. J. W. Mason & J. W. Mason (Chichester: Praxis Publishing Ltd.), 1
 Lueber, A., Kitzmann, D., Bowler, B. P., Burgasser, A. J., & Heng, K. 2022, *ApJ*, **930**, 136
 Luna, J. L., & Morley, C. V. 2021, *ApJ*, **920**, 146
 MacDonald, R. J., & Lewis, N. K. 2022, *ApJ*, **929**, 20
 MacDonald, R. J., & Madhusudhan, N. 2017, *MNRAS*, **469**, 1979
 Macintosh, B., Graham, J. R., Barman, T., et al. 2015, *Sci*, **350**, 64
 Madhusudhan, N. 2012, *ApJ*, **758**, 36
 Madhusudhan, N., & Seager, S. 2009, *ApJ*, **707**, 24
 Marley, M. S., Saumon, D., Guillot, T., et al. 1996, *Sci*, **272**, 1919
 Marley, M. S., Saumon, D., Visscher, C., et al. 2021, *ApJ*, **920**, 85
 Marois, C., Macintosh, B., Barman, T., et al. 2008, *Sci*, **322**, 1348
 McKay, C. P., Pollack, J. B., & Courtin, R. 1989, *Icar*, **80**, 23
 Metchev, S. A., Heinze, A., Apai, D., et al. 2015, *ApJ*, **799**, 154
 Miles, B. E., Biller, B. A., Patapis, P., et al. 2022, arXiv:2209 arXiv:2209.00620
 Mollière, P., Molyarova, T., Bitsch, B., et al. 2022, *ApJ*, **934**, 74
 Mollière, P., Stolker, T., Lacour, S., et al. 2020, *A&A*, **640**, A131
 Mollière, P., Wardenier, J. P., van Boekel, R., et al. 2019, *A&A*, **627**, A67
 Morley, C. V., Fortney, J. J., Marley, M. S., et al. 2012, *ApJ*, **756**, 172
 Nissen, P. E. 2013, *A&A*, **552**, A73
 Nissen, P. E. 2015, *A&A*, **579**, A52
 Nixon, M. C., & Madhusudhan, N. 2022, *ApJ*, **935**, 73
 Öberg, K. I., Murray-Clay, R., & Bergin, E. A. 2011, *ApJL*, **743**, L16
 Perry, J. J., Kim, Y. H., Fox, J. L., & Porter, H. S. 1999, *JGR*, **104**, 16541
 Pineda, J. S., Hallinan, G., & Kao, M. M. 2017, *ApJ*, **846**, 75
 Pineda, J. S., Hallinan, G., Kirkpatrick, J. D., et al. 2016, *ApJ*, **826**, 73
 Radigan, J., Jayawardhana, R., Lafrenière, D., et al. 2012, *ApJ*, **750**, 105
 Radigan, J., Lafrenière, D., Jayawardhana, R., & Artigau, E. 2014, *ApJ*, **793**, 75
 Richard, C., Gordon, I. E., Rothman, L. S., et al. 2012, *JQSRT*, **113**, 1276
 Richey-Yowell, T., Kao, M. M., Pineda, J. S., Shkolnik, E. L., & Hallinan, G. 2020, *ApJ*, **903**, 74
 Saumon, D., & Marley, M. S. 2008, *ApJ*, **689**, 1327
 Saumon, D., Marley, M. S., Abel, M., Frommhold, L., & Freedman, R. S. 2012, *ApJ*, **750**, 74
 Schwarz, G. 1978, *AnSta*, **6**, 461
 Smart, R. L., Tinney, C. G., Bucciarelli, B., et al. 2013, *MNRAS*, **433**, 2054
 Sorahana, S., Yamamura, I., & Murakami, H. 2013, *ApJ*, **767**, 77
 Suárez, G., & Metchev, S. 2022, *MNRAS*, **513**, 5701
 Tan, X., & Showman, A. P. 2021, *MNRAS*, **502**, 678
 Toon, O. B., McKay, C. P., Ackerman, T. P., & Santhanam, K. 1989, *JGR*, **94**, 16287
 Tsuji, T. 2002, *ApJ*, **575**, 264
 Vasavada, A. R., Bouchez, A. H., Ingersoll, A. P., et al. 1999, *JGR*, **104**, 27133
 Visscher, C., Ladders, K., & Fegley, B. 2010, *ApJ*, **716**, 1060

- Vos, J. M., Allers, K. N., & Biller, B. A. 2017, [ApJ](#), **842**, 78
- Vos, J. M., Biller, B. A., Bonavita, M., et al. 2019, [MNRAS](#), **483**, 480
- Vos, J. M., Faherty, J. K., Gagné, J., et al. 2022, [ApJ](#), **924**, 68
- Yang, H., Apai, D., Marley, M. S., et al. 2016, [ApJ](#), **826**, 8
- Zalesky, J. A., Line, M. R., Schneider, A. C., & Patience, J. 2019, [ApJ](#), **877**, 24
- Zhang, Y., Snellen, I. A. G., & Mollière, P. 2021a, [A&A](#), **656**, A76
- Zhang, Z., Liu, M. C., Best, W. M. J., Dupuy, T. J., & Siverd, R. J. 2021b, [ApJ](#), **911**, 7
- Zhou, Y., Apai, D., Lew, B. W. P., et al. 2019, [AJ](#), **157**, 128
- Zhou, Y., Apai, D., Schneider, G. H., Marley, M. S., & Showman, A. P. 2016, [ApJ](#), **818**, 176
- Zhou, Y., Bowler, B. P., Morley, C. V., et al. 2020, [AJ](#), **160**, 77